AUTOMATIC METHODS FOR HUMAN EMBRYO COMPONENT EXTRACTION

by

Amarjot Singh

B.Tech, National Institute of Technology, Warangal, 2011

A THESIS SUBMITTED IN PARTIAL FULFILLMENT
OF THE REQUIREMENTS FOR THE DEGREE OF

Master of Applied Science

in the
School of Engineering Science
Faculty of Applied Sciences

© Amarjot Singh 2014
SIMON FRASER UNIVERSITY
Summer 2014

APPROVAL

Name: Amarjot Singh

Degree: Master of Applied Science

Title of Thesis: Automatic Methods for Human Embryo Component Extraction

Examining Committee: Dr. John Jones
                         Associate Professor
                         Chair

                         _____

                         Dr. Parvaneh Saeedi
                         Associate Professor
                         Senior Supervisor

                         _____

                         Dr. Shahram Payandeh
                         Professor
                         Supervisor

                         _____

                         Dr. Ivan Bajic
                         Associate Professor
                         Internal Examiner

Date Approved: _____18th August, 2014_____

Partial Copyright Licence

SFU

Abstract

In this thesis, we proposed two novel methods for blastomere extraction and trophecto-derm segmentation in an attempt to aid physicians in determining embryo's viability. Accurate assessment of embryo's viability can play a vital role towards optimization of in-vitro fertilisation (IVF) treatment outcomes.

The first proposed automatic method is developed to identify blastomeres in human embryo HMC (Hoffman Modulation Contrast) images of day-1 to day-2. Our algorithm applies isoperimetric graph partitioning, followed by a novel region merging algorithm to approximate blastomeres positions. Ellipsoidal models are then used to approximate the shape and the size of each blastomere. The proposed algorithm is evaluated on a dataset of 40 embryo images and it exhibits an average blastomere extraction accuracy of 80%.

The second method segments Trophectoderm (TE) regions in embryos of day-5 (also known as blastocysts) by first eliminating the inhomogeneities of the blastocysts surface using Retinex theory. A level set algorithm is then used to segment TE regions. We have tested our method on a dataset of 85 images and have achieved a segmentation accuracy of 85% for grade A, 89% for grade B and 92% for grade C.

Keywords: In-vitro fertilisation, Blastomeres, Trophectoderm, Embryo viability, Blastocyst.

Acknowledgments

I would like to thank my supervisor, Dr. Parvaneh Saeedi, for all the support, advice and friendship she has given me throughout my studies at SFU. She encouraged creative thinking, provided the necessary freedom, and directed me along the way towards the thesis. Also, many thanks go to my examining committee, Dr. Shahram Payandeh, Dr. Ivan Bajic, and Dr. John Jones for taking time out of their busy schedules to review my thesis and providing invaluable suggestions during my thesis defense. Last but not least, I would also like to thank all my friends and relatives for their help and friendship on my living and studying in Canada. My deepest gratitude goes to my parents who always supported me for over 20 years of school life.

Contents

List of Tables

List of Figures

List of Abbreviations

ART	Assisted Reproductive Technology
CS	Cartesian System
ICM	Inner Cell Mass
IVF	In-vitro Fertilisation
FN	False Negative
FP	False Positive
GT	Ground Truth
HMC	Hoffman Modulation Contrast
LSCF	Least Square Curve Fitting
MP	Multiple Pregnancies
PC	Piecewise Constant
PS	Piecewise Smooth
SET	Single Embryo Transfer
SVM	Support Vector Machine
TE	Trophectoderm
TP	True Positive
ZP	Zona Pellucida

Chapter 1

Introduction

1.1 Introduction

Assisted reproductive technology (ART) came into light with the birth of Louise Brown in 1978. Since the introduction of ART as a treatment for infertility, the number of treatment cycles for couples has steadily increased. In the last two decades, the use of fertility treatment has increased dramatically as a result of a trend toward delayed childbearing. Economic and social climates, as well as pursuit of advanced careers have influenced a significant number of women to defer childbearing to their mid 30s and early 40s. Unfortunately, female reproductive capacity declines from a peak in the second and third decades of life so that by the age of 40 there is a significant reduction in fertility with a high chance of miscarriage. The Canadian Community Health Survey reports that about an average of 13.6% (11.5% to 15.7%) of Canadian women suffer from infertility (data for 2009-2010) which translates to about 900,000 infertile women between ages 18-44.

In-vitro fertilisation (IVF) is a process used to achieve successful pregnancies by fertilizing an egg with a sperm outside the female's body. A key component of IVF treatment offered to infertile couples involves a controlled hormonal hyper-stimulation of the ovaries in order to enable the retrieval of several oocytes (female eggs). After the eggs are retrieved, the semen of the male partner is allowed to liquefy at room temperature and is prepared for fertilization by removing inactive cells and seminal fluid. The eggs are then combined with the sperm in a separate dish that contains special culture medium ready for fertilization. After that the dish is then placed back inside of an incubator. As a result of

fertilization, a zygote is formed. Therefore, the success rate of IVF highly depends on optimal conditions of the culture in the laboratory. In addition, the success rate depends on the methods used for viable embryo (developed during Day 1 to Day 5 IVF process) selection. Currently, the quality of embryos is being analyzed by medical professionals to assess the probability of a healthy fetus from an embryo. Despite the continuous efforts of researchers to optimize existing protocols and procedures, implantation rates for IVF embryos remain relatively low with a clinical pregnancy rate of 30% per transfer [1]. This is partly related to the high variability in developmental competence of the embryos produced during an IVF cycle and difficulties in determining which of the generated embryos has the highest potential leading to live birth. For this reason, IVF clinics across the world often transfer more than one embryo per cycle to increase the odds that a viable embryo will be transferred. While this approach has helped to maintain the current IVF pregnancy rates, it has also led to large numbers of multiple pregnancies (MP). The potentially negative consequences of MPs include pre-eclampsia, maternal haemorrhage, operative delivery, uterine rupture and preterm labour [2]. MPs can easily be prevented by transferring fewer embryos to the patient's uterus, if the quality of embryos can be determined precisely and therefore transferring only the embryo with the highest implantation potential. Multiple pregnancies can be reduced by actively promoting single embryo transfer (SET). The use of SET has increased in clinical practice simultaneously with a requirement for an acceptable pregnancy rate. In order to develop a system capable of effectively selecting the most viable embryos, a strong improvement needs to be made in the current morphological evaluation methods. This results into the need of highly skilled embryologists capable of assessing the quality of embryos or development of an automatic method that will allow less skilled embryologists to assess the quality of embryos with the help of automated systems. The Canadian statistics indicates the number of IVF initiated cycles in Canada for 2007, 2008, 2009, and 2010 are 8,972, 9,868, 10,390, and 11,718 respectively. Each cycle of IVF cost an average of CAD $ 11,000. Despite the availability of this procedure in most places these days, its high cost limits the number of time that a couple can afford to use this procedure as an infertility option. Here, we hope to develop automatic methods to decrease the dependence to expensive and highly skilled embryologists as well as increase the probability of selecting the embryo with the highest implantation rate.
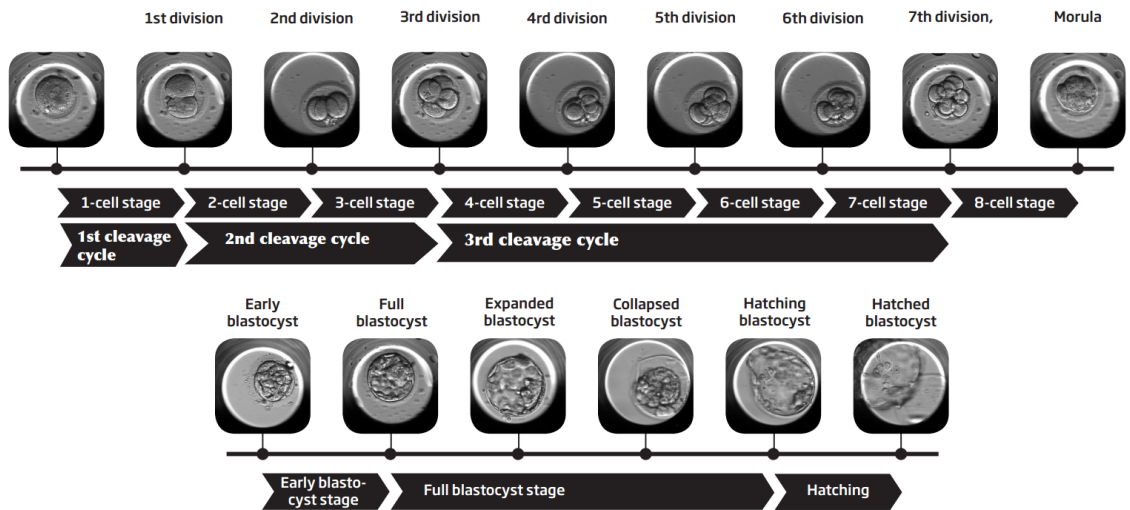
Figure 1.1: Pre-implantation embryonic stages (adapted from [3]).

This dissertation addresses the problem of automatic identification of two different components of an embryo. We believe this is a step towards developing automated technologies that can assess the quality of an embryo at different stages of its growth outside the patient's body and help to grade it using its morphological characteristics. Following sections will provide an overview of the pre-implantation embryo development. Additionally, a review of current embryo grading techniques, followed by the difficulties faced by these methods are presented. Finally, the aim and objective of this thesis are discussed.

1.2 Development of the Pre-implantation Embryo

Fertilization is the first step in human embryo development. Fertilization is produced on penetration of spermatozoon through the extracellular multilayer glycoprotein membrane known as the zona pellucida (ZP). The spermatozoon membrane further fuses with the oocyte membrane to produce a fertilized oocyte [4]. Once fertilized, the oocyte is denoted as zygote (1-cell stage) as shown in Fig. 1.1. Next, zygote enters into its first mitotic division resulting into two embryonic cells known as first clevage. The 1st cleavage cycle is completed with the 1st division early on day 2, about 24-29 hours after fertilization [5]. The two embryonic cells divide during the 2nd and 3rd cleavage cycles, forming a 3 and a 4 cell embryo on day 2. Further cleavages result in the formation of more than 4 cells, followed

by a final round of cell divisions, before the embryo starts compacting into a morula on day 4. Shortly after the morula stage a fluid filled cavity develops. This cavity, also known as the blastocoel, defines the blastocyst stage [4]. On day 5, the embryonic cells differentiate and turn into the inner cell mass (ICM), which will later develop into the fetus, and the trophectoderm (TE), respectively which later creates the plecenta. TE is responsible for the formation and subsequent expansion of the blastocoel [6]. Escape of the mammalian embryo from the surrounding zona pellucida (ZP), referred to as hatching, usually occurs on day 5-6. An outline of the cellular and embryonic stages of a human embryo development is presented in Fig. 1.1.

1.3 Embryo Grading

Embryo examination and grading have resulted in an improved success rate of pregnancies in IVF over the past few years. In addition, embryo grading has reduced the number of transferred embryos leading to multifetal pregnancies. Grading systems currently use developmental rate and cell morphology to assess the quality of embryos. In order to assess the viability, embryos are removed tentatively from the incubator and observed under the microscope at a few, discrete and well defined inspection times [7]. Despite the varied embryo grading schemes used by different fertility clinics, most laboratories grade embryos based on the degree of fragmentation, presence and number of nuclei and size, number and symmetry of blastomeres. On the other hand, blastocysts are primarily evaluated with respect to the expansion of the blastocoels and the number and cohesive property of cells in the ICM and TE [8]. However, all different scoring systems can be grouped into three main systems: zygote, cleaved embryo and finally blastocysts scoring systems [9].

1.3.1 Zygote Scoring System

In the zygote scoring system, the evaluation is performed 16-18 hours after fertilization and it evaluates the pronuclear size and symmetry, size, number, quality and distribution of nucleoli and appearance of cytoplasm as shown in Fig. 1.2. The most popular system was introduced by Scott *et al.* [10] that has been widely accepted and reported for its usefulness in the selection of good embryos leading to better implantation rates. This system uses five grades based on both number and distribution of nucleoli in the pronuclei described in
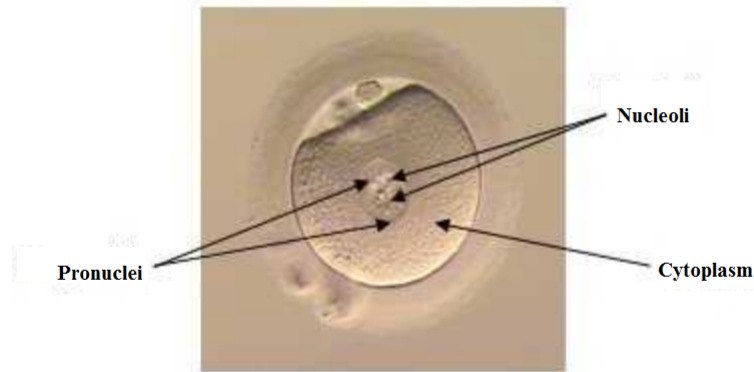
Figure 1.2: Pre-implantation embryonic stages.

Table 1.1: Grades are based on number and distribution of nucleoli in the pronuclei.

Grade	Definition
1	Equal numbers of nucleoli aligned at the pronuclear junction. The absolute number of nucleoli ranges between three to seven.
2	Equal numbers of nucleoli of equal size in the same nuclei but one nucleus having alignment at the pronuclear junction and the other with scattered nucleoli.
3	Equal numbers and sizes of nucleoli which are equally scattered in the two nuclei.
4	Unequal numbers and/or sizes of nucleoli.
5	Pronuclei that are not aligned.

Table. 1.1.

According to the experiments performed by Scott *et al.* [10], 49.5% of zygotes with equal number of nucleoli resulted into blastocyst formation while this number was only 29% for zygotes with unequal number of nucleoli. Hence, zygotes of grade 1, 2 and 3 are preferred for IVF implantation.

1.3.2   Cleaved Embryos System

In the cleaved embryos system, features including (i) Number of cells (blastomeres) (ii) Appearance and size of blastomeres (iii) Cytoplasm defects (fragments) are evaluated 40-48 hours after fertilization. These features are shown in Fig. 1.3.
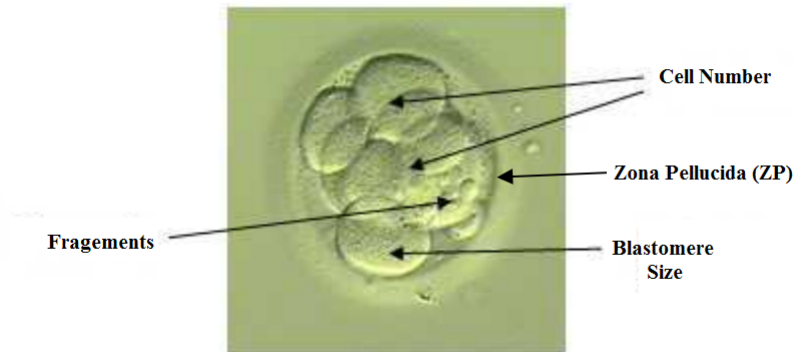
Figure 1.3: Pre-implantation embryonic stages.

The Cleaved Embryo system has been adopted by many researchers including Puissant et al. [11], Staessen et al. [12], Steer et al. [13] and Zeibe et al. [14]. However, several other grading techniques have been introduced by other research groups, and many clinics use their preferred grading system. Puissant et al. [11], for example, used the scoring technique shown in Table. 1.2.

Table 1.2: Embryo Scoring.

Score	Definition
1	Fragments over >1/3 of embryonic surface.
2	Embryos with more fragments but over <1/3 of the embryonic surface.
3	Embryos with few or no fragments but with unequal blastomeres (>1/3 difference in size).
4	Embryos with clear, regular blastomeres and either no fragmentation or a maximum of five small fragments.

According to the experiments performed by Puissant et al. [11], 32% of the embryos with grade 3 or 4 successfully resulted into a fetus, while this number was only 21% for embryos with grades 1 or 2. Hence, embryos of grades 3 or 4 are preferred over embryos of grades 1 or 2.

On the other hand, Zeibe et al. [14] graded embryos based on morphological criteria as described in Table. 1.3.

According to the experiments performed by Zeibe et al. [14], the implantation rate (21%)

Table 1.3: Embryo grading based on Morphology.

Morphology Score	Definition
1.0	Equally-sized symmetrical blastomeres.
2.0	Uneven sized blastomeres.
2.1	Embryos with 10% fragmentation.
2.2	Embryos with 10-20% fragmentation.
3.0	20-50% blastomeric fragmentation.
4.0	50% blastomeric fragmentation.

and pregnancy rate (43%) after transfer of embryos of score 1.0 were significantly higher than that of embryos of score 2.0 (14 and 32% respectively). Transferring embryos of score 2.1 resulted in significantly higher implantation rates (26%) as compared to embryos with score 1.0. Transferring embryos of score 2.2-3.0 resulted in a significantly lower implantation (5%) and pregnancy (15%) rates. Another important finding was that embryos of quality score 2.0 had a significantly lower implantation rate compared to embryos with quality scores of 1.0 and 2.1 with significantly lower pregnancy rates compared to embryos of quality score 1.0.

The authors also analyzed the implantation and pregnancy rates with respect to the number of blastomeres or cells in an embryo. The transfer of 4-cell embryos resulted in significantly higher implantation and pregnancy rates (23 and 49%) compared to 2-cell and 3-cell embryos. Furthermore, the transfer of 4-cell embryos resulted in a significantly higher pregnancy rate compared to embryos that had cleaved beyond the 4-cell stage. From these experiments it was concluded that the pregnancy rate is only acceptable for 2-4 cell or day 1-3 embryos and decreases beyond day-3 embryo images. The suboptimal performance of embryos developed beyond day 3, has led many clinics to maintain their day 2 or day 3 embryo transfer practice. The reasons for this high rate of embryonic loss during early development are unclear, but could include chromosomal abnormalities, suboptimal culture conditions or inadequate oocyte maturation.

1.3.3 Blastocysts Scoring System

A blastocysts scoring system grades embryos on day 5 of their development. The day 5 stage is also known as blastocyst stage. This system grades the viability of embryos based

on the level of expansion of ZP, TE cell layer and ICM cells enclosing a fluid filled cavity as shown in Fig. 1.4.
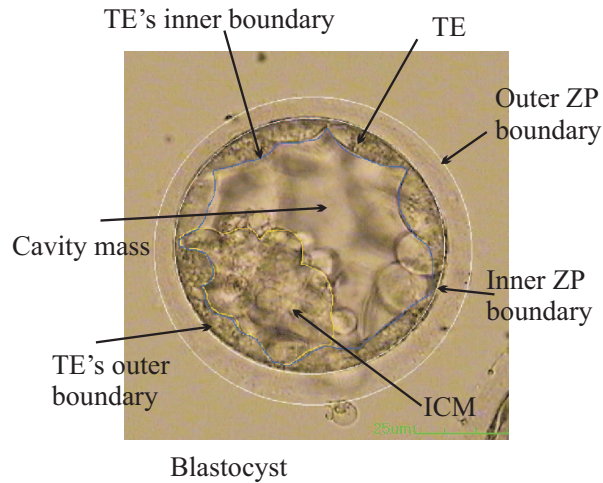
Figure 1.4: Human embryo on day 5 (blastocyst stage) of its creation.

The blastocyst embryo grading systems proposed by Dokras *et al.* [15] and Gardner *et al.* [8] have been widely accepted for blastocyst grading. Dokras *et al.* [15] uses blastocoel's development rate and its characteristics to grade an embryo. The embryo is graded as BG1, BG2, or BG3. On the other hand, Gardner *et al.* [8] focuses on blastocoel size and developmental characteristics of the ICM and TE to grade the blastocyst. First, a blastocyst is graded from 1 to 6 according to its level of ZP expansion. Next, the blastocyst is graded further using the characteristics of ICM from A to C with A being the best score and C being the worst. Finally, it is graded according to the quality of TE. A is associated with the best grade while C is associated with the worst score as shown in Table. 1.4.

Despite the large number of published studies, there is no agreement on the most accurate method for embryo grading. The grading systems adopted mostly rely on factors such as the embryologists, knowledge, experience and the IVF clinic by itself. However, for the work in this thesis, we aim to propose a system capable of automatically extracting the features used to grade an embryo. Here, we will not be grading an embryo, rather we automatically segment different components of an embryo to allow eventually, automatic grading by machine using a sequence of images instead of discrete and scattered observations.

Table 1.4: Gardner's system (top) embryo development grading (bottom) ICM and TE grading

Grade	ZP grade or Expansion quality
1	Blastocoel cavity less than half the size of embryo.
2	Blastocoel cavity more than half the size of embryo.
3	Blastocoel cavity completely filling the embryo.
4	Blastocoel cavity larger than that of early embryo.
5	Hatching out of ZP.
6	Hatched out of ZP.

Grade	TE quality
a	Many cells in a cohesive layer.
b	Few cells in a loose epithelium.
c	Very few large cells.
Grade	ICM quality
A	Many tighly packed cells.
B	Several loosely grouped cells.
C	Very few cells.

1.4 Thesis Objective

The main objective of this thesis is to develop an intelligent system to identify and segment blastomeres in day 1-day 2 human embryos as well as TE region in blastocyts. This potentially can help embryologists in selecting the embryo with the highest probability of implantation. Successful implantation of an embryo depends on the development of embryo on day 1, 2, 3 and 5. Size and shape of blastomere on Day 1, 2 and 3 are strong indicators of the embryo viability. The probability of an embryo producing a fetus also highly depends on the thickness of TE in blastoceol (Day 5). Hence, we aim to design a system capable of identifing the blastomers from day-1 to day-2 and TE from day 5 embryo images.

Blastomere extraction is a complex problem due to fragmentation in embryo images. In addition, overlapping and irregularly shaped blastomeres could increase the complexity of the recognition problem as shown in Fig. 1.5. The first row shows blastomere images with different percentage of fragmentation. The second row depicts images with different
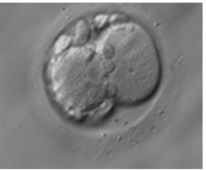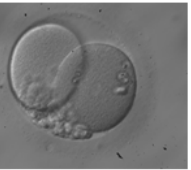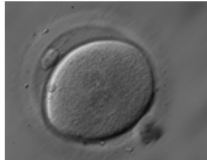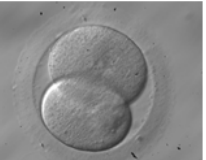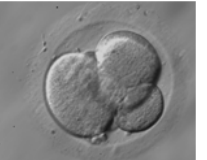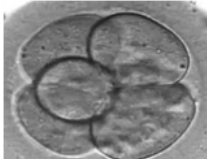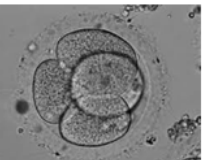
Characteristic	Example			
Fragmentation				
Number				
Size	Even		Uneven	

Figure 1.5: Examples of day 1-day 2 embryos with different qualities.

number of blastomeres. Finally, the third row presents the blastomere with even and uneven sizes.

TE segmentation analysis is also a vital part of many embryo grading systems. The complex nature of patterns and shapes of an embryo makes it very difficult to segment the TE regions as depicted in Fig. 1.6. The first row of this figure showcases blastocysts with TE containing a large number of cells in the cohesive layer. In addition, the TE is clearly differentiable from ICM. The second row presents examples in which TE is connected to the ICM. The third row shows blastocyst images with TE containing only few cells in the cohesive layer.
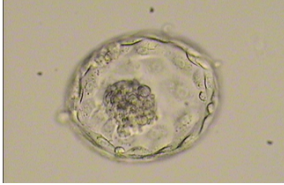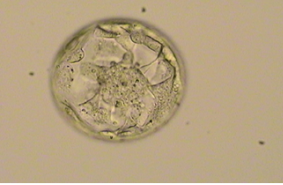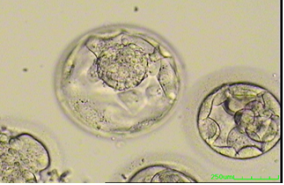
Characteristic	Example		
TE is separarated from ICM			
TE and ICM are attached			
Weak TE			

Figure 1.6: Examples of blastocyst embryo quality.

1.5   Contributions

In this work, two contributions have been made:

1. We proposed and implemented an automatic blastomere identification and modelling approach in an attempt to aid IVF scientists in determining embryo's viability. This method uses isoperimetric graph partitioning to segment the image into approximate blastomere regions. The false regions are merged using a novel region merging algorithm, and further ellipsoidal models are employed to approximate the shape and the size of blastomeres.

2. We developed a fully automatic method for segmentation and measurement of TE region in day 5 human embryos. This system can be further used to compute the width of the TE, which can be useful for automatically training and grading TE quality [16].

1.6   Thesis Organization

The remainder of the thesis is divided into four chapters. Chapter 2 presents our proposed graph based algorithm that is used to approximate the shape and the size of blastomeres. Chapter 3 details the proposed partial differential equation based algorithm for TE segmentation. Finally, Chapter 4 presents the conclusion along with suggestions for future work.

Chapter 2

Blastomere Detection

Fertility specialists have linked size, shape and position of blastomeres in humans embryos with the viability of such embryos [17]. Such parameters play a vital role in manual embryo grading. The most common approach used for estimating these parameters includes observation and measurement of such parameters using digital 2D microscopic images of embryos. These images represent the embryo, a 3D-like translucent side-lit structure, in a 2D form that is easy for human interpretation, as shown in Fig. 2.1. Difficulties arise with automatic image analysis because of the side-lit nature of HMC images, as well as partial or full overlaps between blastomeres, cellular fragmentation, and irregular shapes and sizes.

A handful of attempts have been made to automatically segment blastomeres using 3D modeling approaches. Wong *et al.* [18] presented an automatic tracking method based on particle filter to track the cleavage of embryos. Tian *et al.* [19] proposed a preprocessing method to obtain part of singly connected blastomere edges from a single embryo image. Least square curve fitting (LSCF) method was further applied on these edges to automatically extract blastomeres. Pedersen *et al.* [20] proposed a 3D modeling system for blastomeres through Z-stack images using a multiphase variational level set with manually extracted contours. Giusti *et al.* [21] proposed a system for analyzing blastomeres (cells in day 1 to day 3 of the embryo's development) using 3D volumes of microscopic HMC embryo images. Both methods required upwards of 20 images at various focus levels to complete an entire model for one embryo. They first transfered each image to an acyclic graph associated with a predefined energy. By searching for the path of lowest energy, the 3D contour generator curve was found. Thus the segmentation was achieved.

13
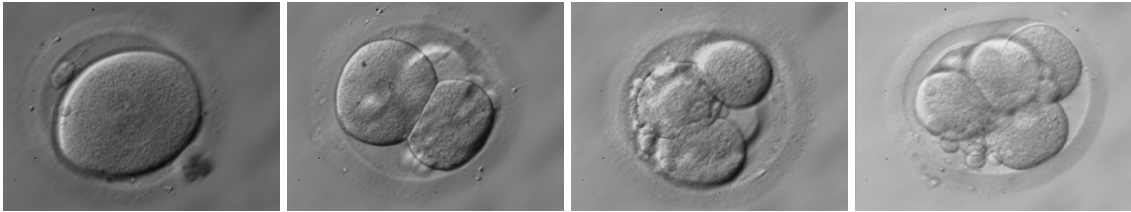
Figure 2.1: HMC images for different blastomere categories (a) one cell (b) two cells (c) three cells (d) four cells.

Here, we propose a novel method for segmenting blastomeres during day 1 and day 2 of the embryonic development using a single image, thus reducing the computational complexity. The algorithm uses a graph partitioning and region merging method followed by a model based shape fitting technique to extract blastomeres in an attempt to aid physicians in determining embryo's viability. We discuss experimental results on a dataset of 40 embryo images, and expand on the advantages and drawbacks of our method while comparing our method to other approaches.

The chapter is divided into the following sections. Section 2.1 describes the proposed algorithm. Section. 2.2 presents the implementation of the algorithm. Section. 2.3 illustrates the details of the dataset used for the experimentation. Finally, Section 2.4 presents the step-by-step experimental results leading to blastomere segmentation.

2.1 Proposed Algorithm

The blastomere extraction algorithm proposed in this chapter comprises four components. The first component segments the image into regions that correspond to the blastomeres using isoperimetric graph partitioning. Due to non-uniform illumination while imaging and cellular fragmentation within each embryo, the resulting regions (we refer to them as partitions) might not correspond to a complete blastomere. To obtain regions that each correspond to one complete blastomere, we propose the second component of the algorithm, a novel region merging algorithm that utilizes length, vesselness [22], and entropy [23] of the borders between regions. These regions are good indicators of the position of blastomeres; however, accurate blastomere shapes are required. To represent blastomeres shapes, the third and the final step of the algorithm utilizes candidate ellipsoidal models that are fitted to the edges of the image via a least-squares fitting approach. Among all found candidates,
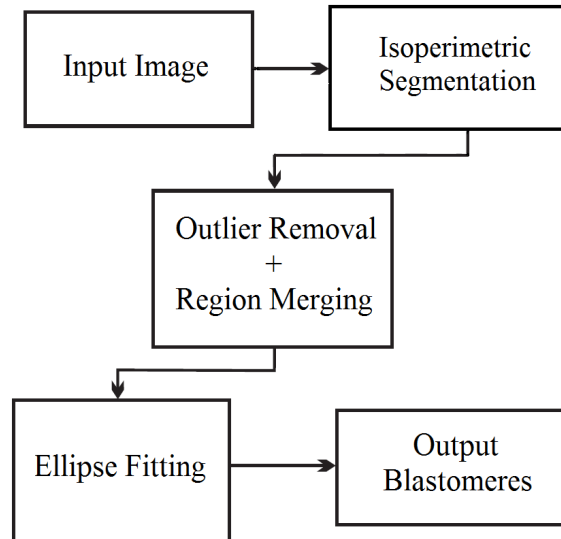
Figure 2.2: Proposed system's flowchart for blastomere identification.

those that best represent combinations of merged regions are selected. A couple of physical constraints are used to further filter outlying candidates. These physical constraints include the minimization of the unused space within an embryo and a state of equilibrium. Fig. 2.2 displays the block diagram of the proposed method. Details of each process are presented next.

2.1.1 Isoperimetric Segmentation

This section details the application of isoperimetric graph segmentation for blastomere extraction on HMC human embryo images. In order to better understand isoperimetric graph segmentation, the fundamentals of graph-based segmentation are provided followed by details of isoperimetric graph segmentation.

2.1.1.1 Graph Partitioning

Graph partitioning, originally introduced by Boykov and Kolmogorov [24], aims to select subsets of graph vertices such that the subsets share a minimal number of spanning edges. Graph partitioning uses min-cut algorithm to segment image graphs into vertex subsets (foreground and background) while satisfying a certain cardinality constraint. An example

(a) Foreground Seeds **(b) Background Seeds** **(c) Uncertain region**
(d) Foreground Marker **(e) Background Marker** **(f) Graph Cut result**
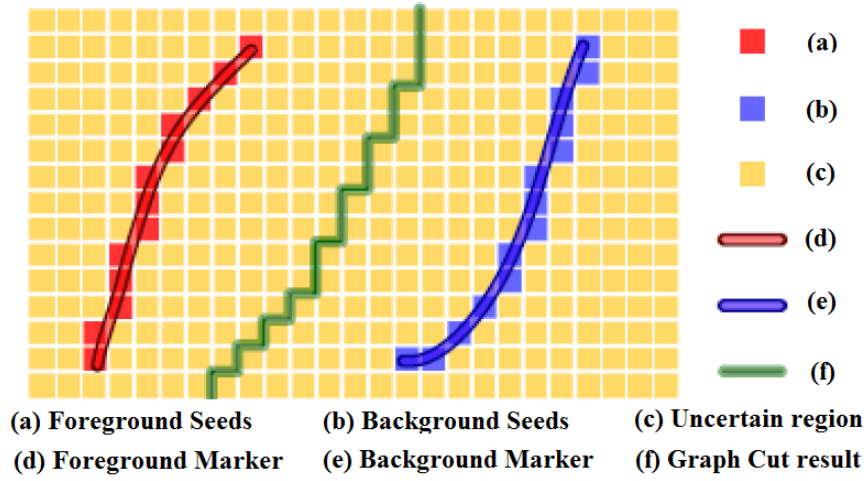
Figure 2.3: Foreground and background is labelled using wide brush strokes. Hard constrained segmentation is accordingly performed using the foreground and background seed pixels.

of the image to be segmented is presented in Fig. 2.3. The example shows an object present in front of a background. The user marks the "foreground" and "background" pixels using free-form, wide-brush strokes. The system uses the marked pixels as foreground and background seeds to perform image segmentation.

Once the object to be segmented is labelled by the user, image segmentation framework classifies any image pixel p to either the foreground or the background. The label assigned to the image pixels are stored in the label vector X as mentioned below:

$$X = x_p, \ where \ x_p \in \{frg, bkg\} \tag{2.1}$$

For an optimal segmentation the label vector X should result in the minimization of an energy function that is defined by:

$$E(X) = (1 - \lambda) \sum_{p \in P} E_1(x_p) + \lambda \sum_{\substack{p,q \in N \\ x_p \neq x_q}} E_2(x_p, x_q) \tag{2.2}$$

In the above equations, P represents the set of all image pixels, N is the set of neighbouring pairs of pixels (8-connectivity chosen), E_1 is called the region term, E_2 the boundary term, and λ a constant that controls the relative significance of the two terms. For

a given labelling, $x_p \in (frg, bkg)$, $E_1(x_p)$ is low if p indeed fits to be a foreground/ background pixel as segmented. For two adjacent pixels with different labels $p, q \in N$, $x_p \neq x_q$, $E_2(x_p, x_q)$, is low if p and q have high grayscale differences, which implies they're indeed fit to represent a border. A soft constraint can be used for the border pixels, however the pixels marked by the user should necessarily follow the $hard\ constraint$. Hence, the resulting segmentation should hold the following labels:

$$\forall p \in F,\ x_p = frg\ \ (foreground)$$
$$\forall p \in B,\ x_p = bkg\ \ (background)$$

(2.3)

Where F (and B) are the user marked foreground (and background) pixels respectively.

2.1.1.2   Segmentation as a Graph Cut

The image is now treated as an undirected weighted graph $G \in (V, E)$ where for each pixel p there exists a node in V, and for each 8-connectivity pixels-pair there exists an edge in E. Two special terminal nodes called source and sink were added to present "*foreground*" and "*background*", respectively. Edges were added from each pixel-node to the two terminal nodes. The edges between neighbouring pixels are represented by *n*-links [24] while edges from a pixel-node to a terminal node are denoted by *t*-links as shown in Fig. 2.4.

A cut in a graph is the subset of the edges that, if removed, splits the graph into two sub-graphs. The cost of the cut is measured by the sum of weights of the cut edges. The minimal cut is the cut with minimal sum-of weights out of all possible cuts. The problem of finding a minimal cut is closely related to the max-flow problem. Max-flow method can segment the graph in low order polynomial time to obtain a globally optimal solution [25]. Each possible image graph segmentation can be described as a cut that separates the source (*foreground*) from the sink (*background*). The minimal cut will generate the optimal segmentation with respect to the properties built into the edge weights. In order to obtain the best segmentation, correct weights need to be selected that will result in minimization of Equation. 2.2.
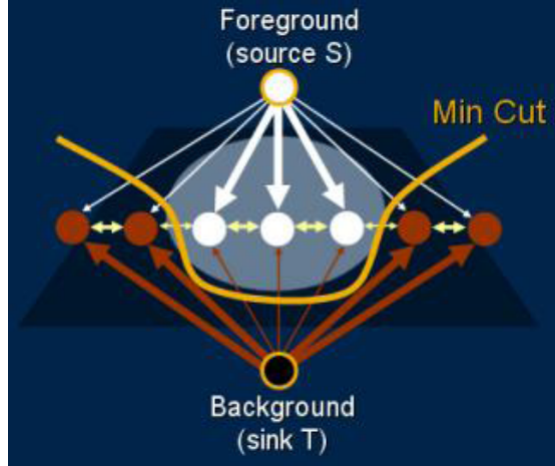
Figure 2.4: Foreground/Background pixel nodes are marked in white/brown (resp.). The source and sink terminal nodes are drawn outside the image. *n*-links are drawn in yellow and *t*-links in white/brown. Links with high weight are shown thick. Min-Cut algorithm best separates the source, with all the foreground pixels, from the sink, with all the background pixels.

2.1.1.3 Defining the Edge Weights

Edge weights should reflect the soft as well as the hard constraints. The soft constraints should reflect the probabilities that a specific "unmarked" pixel p belong to either foreground or background. These probabilities are based on the pixels that the user labelled initially. These probabilities are estimated by using the foreground and background marked pixels to generate the normalized histograms $H_{frg}(I)$ and $H_{bkg}(I)$, respectively. The hard constraints should be reflected in very high/very low edge weights that will force the marked pixels to be in the desired side of the cut.

p	$w(p, S)$	$w(p, T)$
$\forall p \in F$	K	0
$\forall p \in B$	0	K
$\forall p \in U$	$-\ln H_{bkg}(p)$	$-\ln H_{frg}(p)$

Table 2.1: Graph Cut Table

Next, the arc weights for the *t*-links of both hard and soft constraints are defined in Table. 2.1. K, is a large enough constant that is not included in the minimal cut. Note that $U = P - (F \cup B)$ is the set of uncertain pixels to be segmented. To better understand Table.
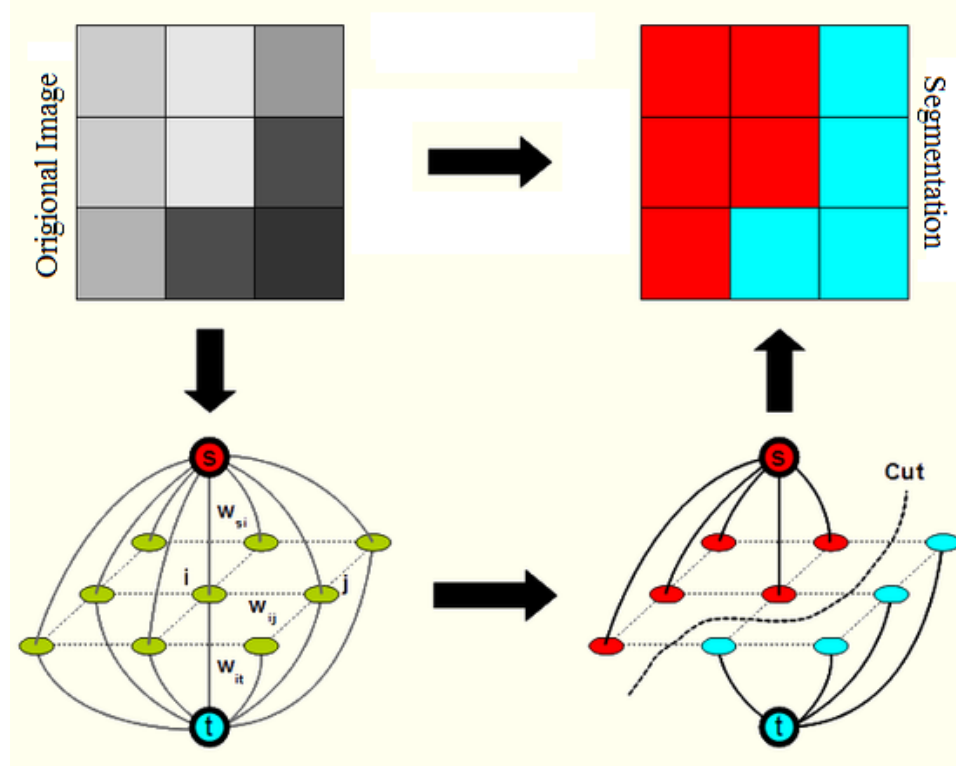
Figure 2.5: Defining the edge weights. (a) User marks only one seed pixel for foreground and one for backgrounds (marked O and B respectively) (b) A Weighted graph is generated. Weights for t-links to background terminal node T and for n-links are shown (t-links to foreground terminal S are equivalent). (c) Minimal cut. (d) Imposed segmentation.

2.1, consider an example with a pixel p with high probability to be classified as foreground frg, where $H_{frg}(p)$ is relatively high. As a consequence $-\log H_{frg}(p)$ will be relatively small resulting in a lower weight on p in *t*-link. In the final segmentation, this edge will have a higher probability of belonging to the cut. Therefore, p is detached from T and placed in S side (*foreground*) of the cut. The graph segmentation process is presented in Fig. 2.5. In order to correctly separate between pixels that have opposite frg/bkg labels, we must give such neighbouring pairs a low-cost weight on their link (so their connecting edge will be included in the cut). The following cost function assigns a low cost to pixels with different intensities:

$$W(p,q) = \exp(-\frac{(I_p - I_q)^2}{2\sigma^2})\frac{1}{dist(p,q)}, \; where \; x_p \neq x_q \qquad (2.4)$$

Note that here, the normalization is performed based on the distance (dist in Eq. 2.4) between pixels as the adjacent pixels can relate by diagonal directions. The pixels that are far apart have small or zero adjacent weight. Once the adjacent weights are computed, the *n*-links weights are multiplied by λ while the *t*-links weights by (1 - λ), as explained in Equation. 2.2. The minimal cut with respect to the weights will result into the best segmentation according to the overall energy. This is clear from the definition of minimal cut; however, it is also proven mathematically in [24].

2.1.1.4 Isoperimetric Partitioning

Isoperimetric partitioning, proposed by Leo Grady [26], solves a linear system of equations instead of an eigenvector problem for graph partitioning. The isoperimetric algorithm is similar to spectral partitioning in its use and capabilities (e.g., multilevel spectral partitioning [27] and geometric-spectral partitioning [28]). However, it requires the solution to a large, sparse system of equations instead of solving the eigenvector problem for a large, sparse matrix. This contrast in isoperimetric partitioning makes it faster and numerically more stable.

A graph is a pair $G = (V, E)$ with vertices $v \in V$ and edges $e \in E \subseteq V \times V$. An edge, e, spanning two vertices v_i and v_j, is denoted by e_{ij}. Let $n = |V|$ and $m = |E|$ where $|.|$ denotes cardinality. A weighted graph has a coefficient assigned to each edge called a weight. The weight of edge e_{ij}, is denoted by $w(e_{ij})$ or w_{ij}. Since weighted graphs are more general than unweighted graphs (i.e., $w(e_{ij})$ = 1 for all $e_{ij} \in E$ in the unweighted case), all the results are developed for weighted graphs.

Graph partitioning has been strongly influenced by properties of a combinatorial formulation of the classic isoperimetric problem. One such example is finding the shape with minimum perimeter for a fixed area [29]. The approach to graph partitioning used here is a polynomial time heuristic for the NP-hard [30] problem of finding a graph with minimum perimeter for a fixed area. Cheeger [31] defined the isoperimetric constant h of a manifold as:

$$h = inf_S \frac{|\partial S|}{Vol_S} \tag{2.5}$$

where S is a region in the manifold, Vol_S denotes the volume of region S, $|\partial S|$ is the area of the boundary of region S, and h is the infimum of the ratio over all possible S. For a

compact manifold, $Vol_S \leq \frac{1}{2}VolTotal$, and for a noncompact manifold, $Vol_S < \infty$ [30]. For a graph, G, the isoperimetric number, h_G is:

$$h_G = inf_S \frac{|\partial S|}{Vol_S} \tag{2.6}$$

where $S \subset V$ and

$$Vol_S \leq \frac{1}{2}Vol_V \tag{2.7}$$

In finite graphs, the infimum in Equation 2.6 becomes minimum. The boundary of a set, S, is defined as $\partial S = \{e_{ij}| \, i \in S, j \in \bar{S}\}$ and on a weighted graph:

$$|\partial S| = \sum_{e_{ij} \in \partial S} w(e_{ij}) \tag{2.8}$$

In the context of graph partitioning, combinatorial volume is typically taken as:

$$Vol_s = |S| \tag{2.9}$$

For a given set of nodes, S, the ratio of its boundary to its volume is named as the isoperimetric ratio and denote it by $h(S)$. The isoperimetric sets for a graph, G, are any S for which $h(S) = h_G$. A good partition is defined to be one with a low isoperimetric ratio. Therefore, the goal is to maximize Vol_S while minimizing $|\partial S|$. Finding isoperimetric sets is an NP-hard problem [30], and the algorithm used is a heuristic one for finding a set with a low isoperimetric ratio that runs in polynomial time. An indicator vector that takes a binary value at each node is defined by:

$$x_i = \begin{cases} 0, & \text{if } v_i \in S. \\ 1, & \text{otherwise.} \end{cases} \tag{2.10}$$

A specification of x also defines a partition. The $n \times n$ matrix L of a graph is defined as:

$$L_{v_i,v_j} = \begin{cases} d_i, & \text{if } i = j. \\ -w(e_{ij}), & \text{if } e_{ij} \in E \\ 0, & \text{otherwise} \end{cases} \tag{2.11}$$

where d_i denotes the weighted degree of vertex v_i

$$d_{ij} = \sum_{e_{ij}} w(e_{ij}) \, \forall e_{ij} \in E \tag{2.12}$$

The notation L_{v_i,v_j} is used to indicate that the matrix L is being indexed by vertices v_i and v_j. This matrix is also known as the admittance matrix in the context of circuit theory or Laplacian matrix [32].

By definition of L we have:

$$|\partial S| = x^T L x \tag{2.13}$$

and $Vol_S = x^T r$ where r denotes the vector of all ones. Maximizing the volume of S subject to $Vol_S = k$ for some constant $k \frac{1}{2} Vol_V$ may be done by asserting the constraint:

$$x^T L x = k \tag{2.14}$$

The minimum value of the isoperimetric constant h_G for a graph G for minimum value of isoperimetric constant h is defined as:

$$h_G = min_x \frac{x^T L x}{x^T d} \tag{2.15}$$

Here L is the the Laplacian matrix, d is the vector representing nodes degree, and x is the real solution. In order to solve for a particular solution x_0, the node with the largest degree in L is chosen as the ground node v_g. The gth row and column of the Laplacian matrix L are removed and the modified matrix is denoted as L_0. The gth row is represented as x_0, while the vector of nodes' degree is denoted by d_0. Equation (2.15) can be solved as a linear system by reformulating it as a constrained optimization with a Lagrange multiplier. The real solution of x_0 is obtained by solving the following linear system:

$$L_0 = x_0 \times d_0 \tag{2.16}$$

The solution x_0 is classified as foreground or background, if it is greater or smaller than a cut value of α, defined by the user. The process is continued for each segment until the isoperimetric constant value of all partitions becomes smaller than a stop value of 0.05, adopted from the original work in [26].
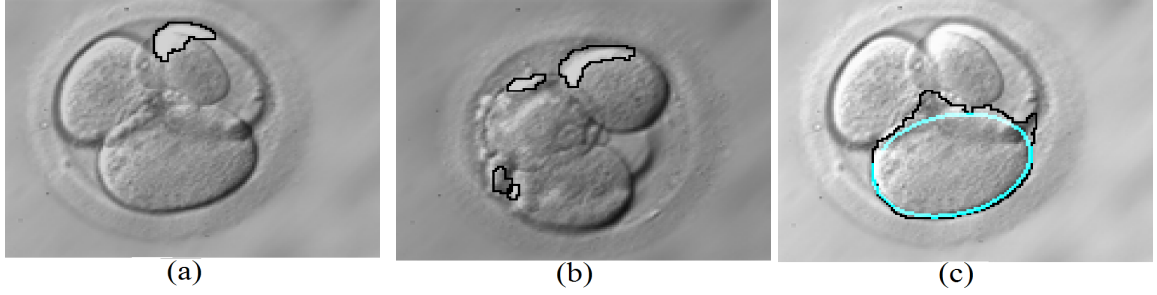
Figure 2.6: Partitions that corresponds to: (a) regions with different brightness values despite being from the same blastomere. (b) Cellular fragmentation. (c) An ellipsoidal hypothesis with the highest border- and area-overlap is a over-imposed on the segmented region.

2.1.2 Proposed Region Merging Algorithm

Any partitioning method including isoperimetric partitioning may produce unwanted partitions within a blastomere due to directional illumination of the subject and/or cellular fragmentation as shown in Figs. 2.6(a) and (b), respectively. To eliminate false partitions, a novel region merging algorithm is introduced. The algorithm uses the length, the entropy [23], and the vesselness of each partition as well as its area to merge partitions. The vesselness is defined by edges and their strength and is computed after enhancing the input image using a multi-scale enhancing filter [22]. Equation (2.17) assigns low *Potential* values to partitions with small areas or short lengths as they more likely correspond to cellular fragmentation or are due to non-uniform illumination of the surface of an embryo. For each partition, the entropy is computed as a measure of the amount of disorder in the image [23] and the vesselness is computed using Frangi's [22]. Once all four attributes are computed for each partition, the *Potential* of each partition is computed by:

$$Potential = 1 - e^{-(\sum_{i=1}^{3} X_i \times W_i) \times area}$$
(2.17)

Here X_i is the attribute (length, entropy and vesselness), W_i is the weight for a specific attribute and $area$ is the area of the region to which the partition belongs to. All partitions with *Potential* values below a merging threshold are removed. In order to estimate the merging threshold and weights in Equation (2.17), we performed test trials on 10 training images. These 10 images are selected from the dataset so that they include 1 to 4 cells. In particular, we have chosen 2 images of one cell, 2 images of two cell, 3 images of three cell and 3 images of four cell embryos. The training dataset contains higher number of training

images for embryos with higher number of blastomeres as these images can have high fragmentation and cell overlaps. This can result into large number of false partitions that essentially requires more examples to capture the variability of the conditions and obtain a better estimate of the weights. Once isoperimetric partitioning segments our images into approximate regions corresponding to blastomeres, the region merging algorithm is applied to merge regions with similar characteristics. The weights in Equation. 2.17 are manually adjusted in order to merge the maximum number of regions. Finally, after taking the average of the optimal weights for all 10 images, we arrived to the weight values of 0.5, 0.3 and 0.2 for length, vesselness and entropy, respectively. We also used these weights to compute *Potential* for each partition using Equation (2.17). The merging threshold was computed by taking the average value of *Potential* of all partitions, which for this work was 0.8.

2.1.3   Ellipse Model Fitting Using Partition Set

The region merging algorithm generated an improved, yet reduced partition set compared to the initial isoperimetric segmentation results; however, these regions are better in indicating the position than the exact shape or profile of the blastomeres. To combat this problem, we propose generating ellipsoidal models from the edge image, then finding the ellipses that best fit our segmented regions.

The edge image is generated by first smoothing the original image using anisotropic diffusion [33]. It is a nonlinear diffusion method that applies an inhomogeneous process on the image to reduce the diffusivity at those locations with higher likelihoods of being edges. This likelihood is measured by $|\nabla u|^2$. The anisotropic diffusion filter is based on:

$$\partial_t u = div(g|\nabla u|^2 \nabla u) \tag{2.18}$$

Next, a Hessian based edge detector [34] is applied to create the edge image. The Hessian edge detector defines an edge on a pixel, if and only if, there are some points in the pixel's neighbourhood that have negative slope zero crossings of the second directional derivative. This derivative is taken in the direction of a nonzero gradient at the pixel's center. All the pixels following this properly are marked as an edge while remaining all pixels are replaced with a zero magnitude edge. Finally, a direct least-squared ellipse fitting algorithm [35] is applied to each pair of edges to produce a set of candidate ellipses. The

best ellipses are chosen as those with the highest percentage border and area overlap with the segmented regions. An example of one such best ellipse (with high border overlaps with the region) is shown in blue in Fig. 2.6(c).

2.1.4   Elimination of False Hypotheses

The set of candidate ellipses consists of true hypotheses representing true blastomeres as well as false ones generated due to noise, fragmentation, cell overlaps, and lighting conditions. Some examples of ellipse candidates generated for different images are shown in Fig. 2.7. The false hypotheses must be removed. Details of the removal procedure are presented next.

(a)   (b)   (c)   (d)
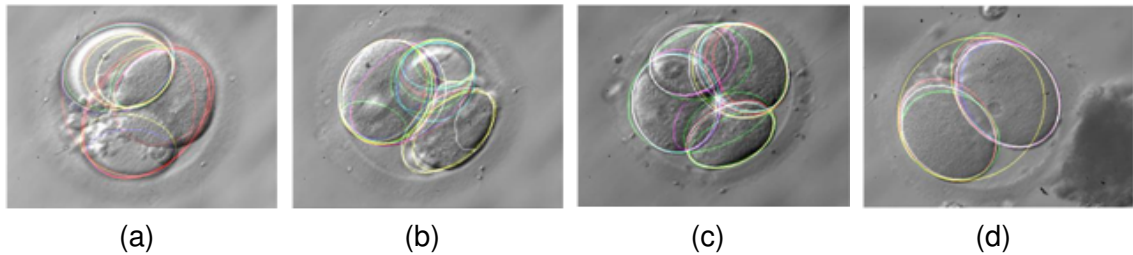
Figure 2.7: Result of ellipse fitting on four sample images.

2.1.4.1   Large Hypotheses Removal

In this part, ellipsoids covering large area of the embryo are removed from the candidate set. In case of one cell embryo images, majority of ellipsoids cover the entire area of the embryo while few ellipsoids may include some background as well. To remove such large ellipses, the image region covered by the entire set of found ellipses is computed. Each ellipse aims to capture a blastomere in the image; therefore all ellipses cover the majority of the embryo area. However, overfitting of some of the ellipses may include certain pixels from the background resulting in a larger area as compared to true blastomeres existing in the image. This difference in area is utilized to remove those large candidates that extend beyond the true area of the embryo. Removal of large hypothesese in embryo images containing more than two blastomeres is presented with an example. Fig. 2.8(a) shows an example of one such case overlapping with more than 50% with the embryo area. The

area of the embryo is estimated by dilating the edge image 100 times followed by an erosion process carried out the same number of times. The estimated area is shown in Fig. 2.8(b).
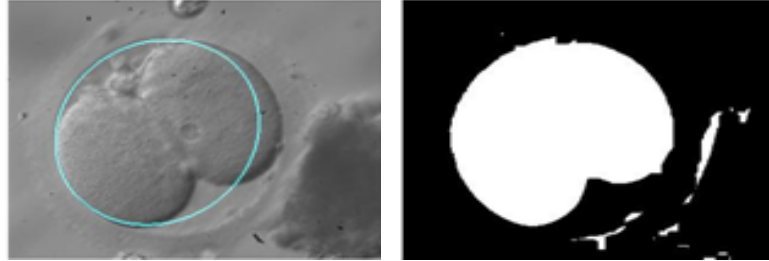
Figure 2.8: (a) A large ellipse hypothesis. (b) Estimated embryo area.

Further, we performed test trials on 10 training images to determine the maximum area covered by an ellipsoid below which it is classified as a true candidate hypothesis. Through these training images, we determined that ellipsoids with an area overlap less than 70% with the embryo area should be in the candidate set. The area covered by an ellipsoid is computed using the following:

$$R_k = \frac{\sum_{i=1}^{M} \sum_{i=1}^{N} H(i,j)}{\sum_{i=1}^{M} \sum_{i=1}^{N} A(i,j)} \times 100 \tag{2.19}$$

Where H is the $M \times N$ hypothesis binary mask, A is the $M \times N$ binary mask of the embryo and R_k is the percent area coverage for hypothesis k. After applying this process to samples shown in Fig. 2.7(d), we will have all the large hypotheses removed while maintaining hypotheses that are more similar to the profile of the true blastomeres that exist in the image, as shown in Fig 2.9.
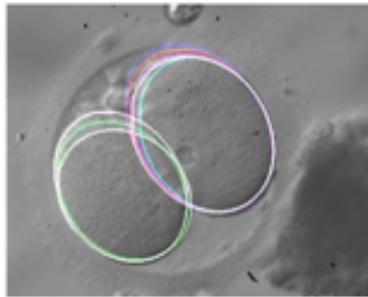
Figure 2.9: Large hypothesis is removed from the ellipse set.

2.1.4.2 Similar Hypotheses Removal

This step removes redundant ellipses that are too similar in shape, size, and spatial location. Similarity between two hypotheses H_1 and H_2 is computed using the following equation:

$$S = \frac{H_1 \cap H_2}{H_1 \cup H_2} \times 100 \tag{2.20}$$

Here H_1 and H_2 are $M \times N$ binary mask of the two hypotheses and S is the similarity measure between hypotheses k_1 and k_2. The smaller hypothesis at the intersection of H_1 and H_2 is removed if S is greater than 95%. An example after the application of this process on the embryo image shown in Fig. 2.7(a) is presented in Fig. 2.10.

(a)   (b)
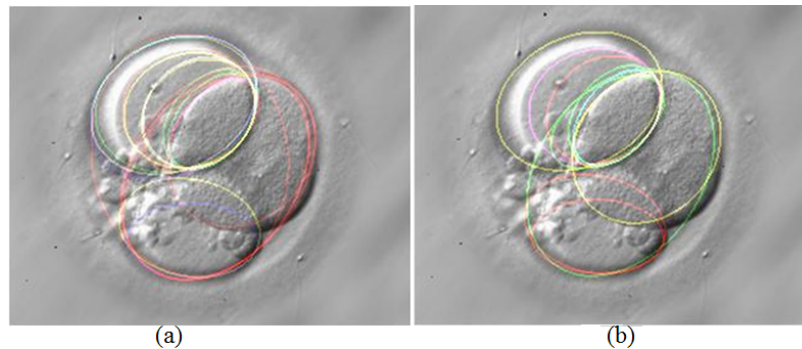
Figure 2.10: Similar hypotheses removed from the set of candidate ellipses: (a) included 21 hypotheses while (b) includes the reduced hypothesis set of 14 ellipses.

2.1.5 Set Based Candidate Selection

The set of ellipses that best represent the merged regions of an embryo must satisfy two physical constraints common to every embryo. These constraints are: (i) The centroid of each embryo is near to the centroid of the polygonal shape defined by the centroids of all candidates. (ii) Blastomeres rarely fully overlap of completely covered fall behind one another, resulting in their 2D views to completely covered or fall inside another cell. As the number of blastomeres in an embryo are unknown, the ellipsoidal models generated in the previous section are grouped into sets that contain 2 to 4 blastomere candidates. The physical constraints are explained in more details in the next section.

2.1.5.1 Centroid Proximity

Blastomeres spatially arrange themselves inside an embryo in a way that minimizes the unused space. We refer to this as the state of the equilibrium. This fact is used to retain equilibrium states with cardinality of 2 to 4 that are distributed evenly throughout the embryonic volume. Examples of such equilibriums for two, three and four blastomeres are shown in Figs. 2.11 (a), (b) and (c), respectively.

<center>(a)   (b)   (c)</center>
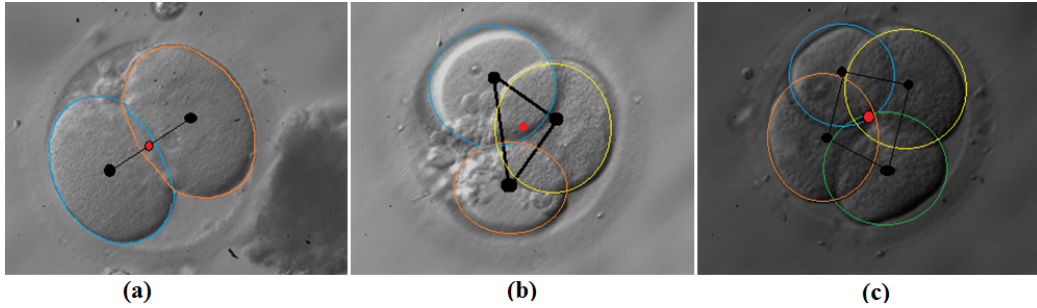
<center>Figure 2.11: Visualization of the state of Equilibrium.</center>

To determine the distribution of the hypotheses within an embryo, a polygon can be constructed out of their centers. For a two blastomere embryo, the constructed shape is a line, for a three blastomere embryo, it is a triangle, and for a four blastomere embryo, it is a rectangle. From Fig. 2.11, it can be observed that the central point of the line, triangle, and rectangle appear to be near to the center of embryo's mass. Although the center point, or midpoint, of a line can easily be found, the center of an irregular polygon often does not exist, because it is unlikely that a point can be found that is equally spaced from each vertex. However, the centroid, or weighted center, of an irregular polygon can be determined. For a non-intersecting, closed polygon with n vertices, $(x_0, y_0).....(x_n, y_n)$, the location of the centroid is defined as (C_x, C_y) [36], where:

$$C_x = \frac{1}{6A} \sum_{i=0}^{n-1} (x_i + x_{i+1})(x_i y_{i+1} - x_{i+1} y_i) \tag{2.21}$$

$$C_y = \frac{1}{6A} \sum_{i=0}^{n-1} (y_i + y_{i+1})(x_i y_{i+1} - x_{i+1} y_i) \tag{2.22}$$

$$A = \frac{1}{2} \sum_{i=0}^{n-1} (x_i y_{i+1} - x_{i+1} y_i) \tag{2.23}$$

The centroid of an equilibrium can be calculated and then compared with the actual center of the embryo in the image. To find the actual center of the embryo, the binary embryo image is used. This image is eroded with a disk structuring element of radius 7 to smooth the outer edges and remove unwanted outer regions not corresponding to actual blastomere. The resulting image is a fully enclosed shape as shown in two examples of Fig. 2.12.

(a)   (b)

(c)   (d)
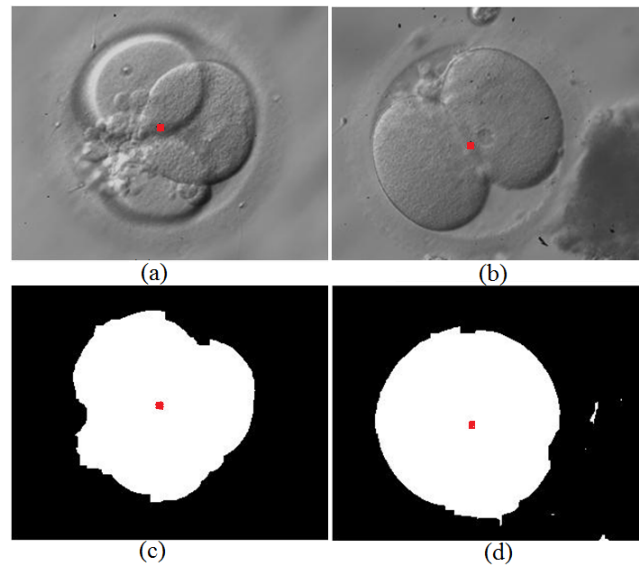
Figure 2.12: (a) Input image (b) It's binary embryo mark with embryo centroid marked with red. (c) Another input image (d) It's Binary embryo mark with embryo centroid marked with red.

Once the centroid of the equilibrium and the embryo mask are generated, the distance between them is used as an indicator to estimate the distribution of equilibrium. For the centroid of the equilibrium, (C_x, C_y), and the centroid of the embryo, (E_x, E_y), the Euclidean distance is used to estimate the distance, d, between the two. It is expected that this distance is minimum for the set that best represent the actual locations of blastomeres. It was experimentally determined that setting a maximum centroid distance of 10 pixels, can help to remove most of the false sets that contradict the equilibrium state.
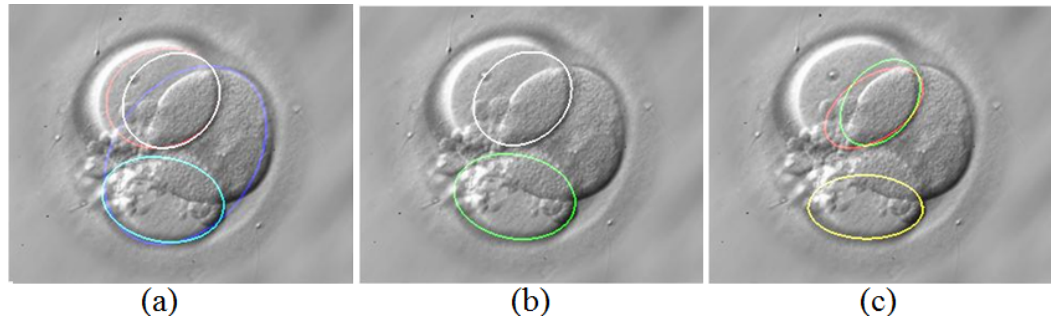
Figure 2.13: The figure shows sample of Equilibriums consisting of 2-4 hypotheses.

2.1.5.2 Contained and Disjoint Hypotheses Removal

To further reduce the number of equilibriums, the characteristics of embryos with two, three, and four blastomeres were taken into consideration. Equilibrium set is further reduced by removing the hypothesis with no or excessive overlap with other hypotheses. This process is based on two very simple principles:

1. Disjointness: There are never disjoint blastomeres in an embryo. For example, in a two blastomere embryo, there will always be an overlap between the two blastomeres.

2. Containment: Blastomeres very rarely fully overlap or contain each other. For example, in a three blastomere embryo, a true blastomere will never fully contain the other two.

Fig. 2.13 provides a range of sample equilibriums generated from the embryo shown in Fig. 2.12(a). These samples are obtained after verification of the centroid constraint mentioned in Section 2.1.5.1. It can be seen that the equilibriums in Fig. 2.13 do not follow the two principles described above. In Fig. 2.13(a), one ellipsoid contains another ellipsoid while in Fig. 2.13(b), both ellipsoids are disjoint. Finally, Fig. 2.13(c) contains both disjoint and as well as contained ellipsoids. As these equilibriums don't follow the characteristics of a true embryo, it is appropriate, that such equilibriums should be found and removed from the set of candidate equilibriums.

The first step taken to remove bad equilibriums is to generate a list of hypotheses that are disjoint and a list of hypotheses that are contained. The disjoint case is when there is a sizeable gap between hypotheses. In some cases there is a very small gap between hypotheses and it must be ensured that such equilibriums are not removed. Also, for

containment, some hypotheses are almost fully contained in another hypothesis. It must be ensured that such equilibriums are removed.

To find disjoint hypotheses the original hypothesis list is used. To account for hypotheses that do not overlap, a morphological process is used that utilizes the binary image of each candidate. The relationship between two binary hypotheses B_1 and B_2 are determined using the following equation:

$$Dis = B_1 \cap B_2 \tag{2.24}$$

B_1 and B_2 are disjoint if Dis is equal to 0%.

To find contained hypotheses, a similar approach is used. Once again, all combinations of two hypotheses are compared. To account for hypotheses that almost fully overlap with each other, the following algorithm has been used:

$$Cont = B_1 \cup B_2 \tag{2.25}$$

B_1 and B_2 are contained if $Cont$ is equal to B_1 or B_2.

2.1.6 Final Equilibrium Selection

The process for selecting the best equilibrium from those remaining, for one to four cell embryo images, utilizes the edgemap of the original image. Ideally, every edge point in the original image should belong to only one hypothesis. For this reason, the amount of the overlap between the boundaries of the equilibirum and the edge map is used as an indicator of the quality of the equilibrium. Therefore, the best equilibrium is selected as the equilibrium with the highest percentage of overlap with the edge image.

To find the best equilibrium that captures the blastomeres in an embryo image, the following operations are applied. In the first step, small connected edges that do not actually correspond to blastomere edges are removed. The raw edge image containing these small edge fragments is shown in Fig. 2.14(a). The edge image is cleaned by removing edges with less than 10 pixels length as shown in Fig. 2.14(b). All the equilibriums are further dilated and overlapped on the cleaned edge image. An example of a dilated binary equilibrium is shown in Fig. 2.14(c). The intersection between the equilibrium boundary and the edge map (for one case) is shown in Fig. 2.14(b). By summing the edge points in
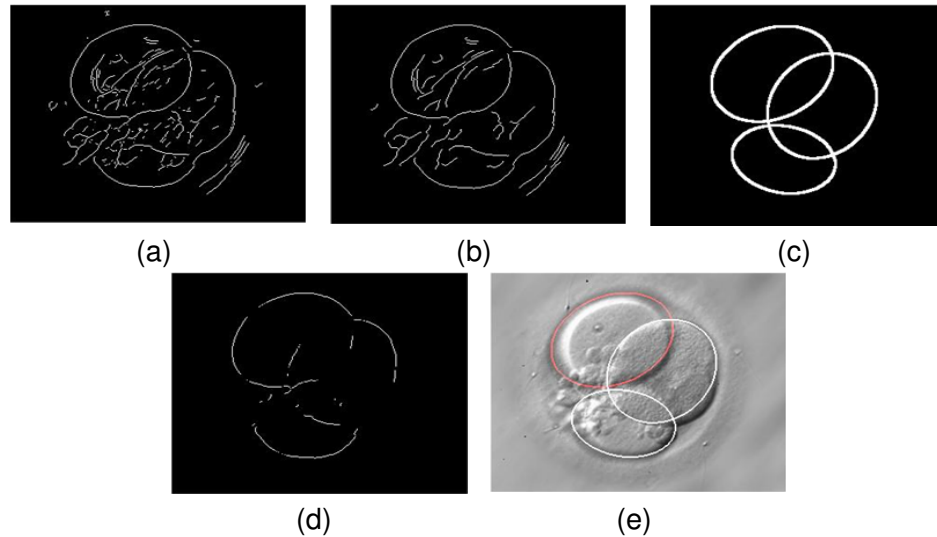
Figure 2.14: (a) Edge representation (b) Refined edge representation (c) Best equilibrium.

Fig. 2.14(d), the percentage of pixels overlapping with the equilibrium are calculated. This process is repeated for all remaining equilibriums and the equilibrium with the highest number of overlap is chosen as the best candidate set. Fig. 2.14(e) shows the best equilibrium set selected by this process.

2.2 Dataset

In order to compute the accuracy of the proposed algorithm, we have used a dataset of 50 HMC human embryo images. The dataset is divided into 10 training and 40 testing images. All the blastomers existing in these images were manually extracted by the authors. We utilize the results of the manual identification as our Ground Truth (GT) and compare the output of our algorithm with those.

2.3 Algorithm Implementation

An HMC embryo image containing three blastomeres, as shown in Fig. 2.15(a), is selected to demonstrate step by step results of the proposed algorithm. In this case, one blastomere is contained within another blastomere. This blastomere in 3D space spatially falls behind the 2D plane at which the image is focused on. As mentioned earlier, our method will not

detect that specific blastomere. Isoperimetric partitioning segments the input image, into 8 regions using a cut value α of 0.6 (Section 2.1) as shown in Fig. 2.15(b). The algorithm successfully segments one blastomere while generates multiple segments within the three remaining. Length, vesselness and entropy along with the area of the regions, to which a partition belongs to are computed in the subsequent step to merge superfluous partitions, as described in Section 2.1.2. Examples of a good (large region on the bottom of the image) and a bad (small region on the top of the image) partition over-imposed on the vesselness and the entropy image are shown in Figs. 2.15(c) and 2.15(d), respectively. The values of vesselness and entropy are shown using intensity mapping. The brightness values in Fig. 2.15(c) represents highly vesseled regions, and the dark regions in Fig. 2.15(d) represents low entropy values.

(a) (b) (c) (d)
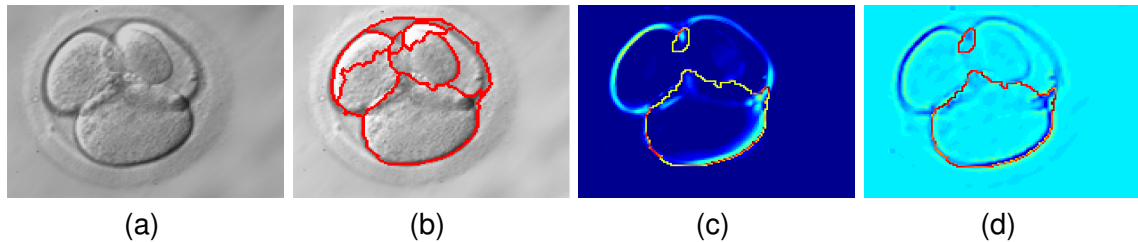
Figure 2.15: (a) Input image. (b) Isoperimetric partitioning of the input image. Values of (c) vesselness, (d) entropy, of the input image.

Fig. 2.16 shows the results for the region merging process. Here, the region merging algorithm has merged three of the seven regions as shown in Figs. 2.16(a) to 2.16(c). Fig. 2.16(d) shows the regions after the merging process is completed.

(a) (b) (c) (d)
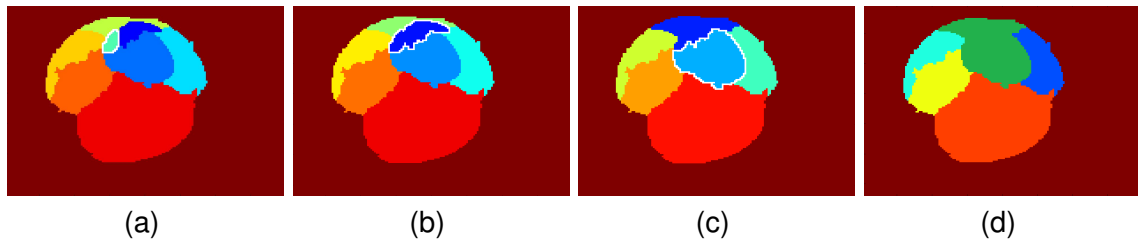
Figure 2.16: Step by step region merging leading to the removal of three of the seven regions using *potential* threshold of 0.8. The regions merged in each step are represented with white border.

Here, the algorithm has not merged the remaining false partitions caused by the non-uniform illumination that resulted in high entropy and gradient values. The ellipsoidal shape of the blastomeres is further exploited to conform each ellipse using a pair of edges

generated via Hessian edge operator, and a least-squared fitting method, as shown in Fig. 2.17(a). All ellipsoidal candidates generated are shown in Fig. 2.17(b). From all generated candidates, we select those that have 90% or more overlap in their areas and boundaries with those of the partitions.

(a)	(b)	(c)
(d)	(e)	(f)
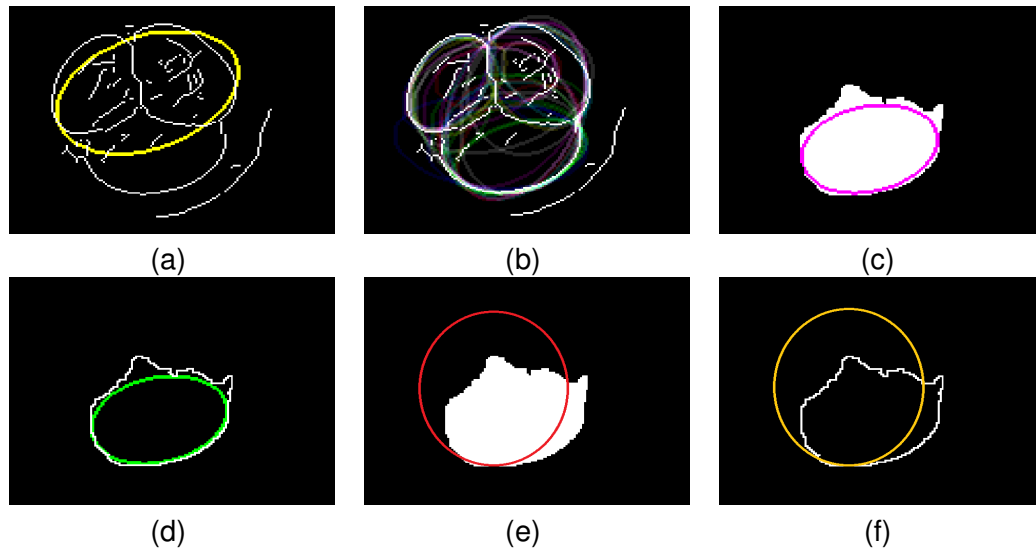
Figure 2.17: (a) Ellipse fitting using least-squared method using an edge pair. (b) Ellipse candidates are generated using all edge pairs. A good ellipse candidate has a large intersection with the segmented regions (c) and their boundaries (d). A bad candidate has smaller region and boundary overlaps as shown in (e) and (f).

Examples of good and bad candidate ellipses are presented in Figs. 2.17(c) to 2.17(f). Figs. 2.17(c) and (d) show an ellipsoidal candidate with more than 90% overlap with the area and boundary values. On the contrary, the area and the boundary overlap of a bad ellipsoidal candidate is small, for the example in Figs. 2.17(e) and 2.17(f). Fig. 2.18 represents some ellipse candidate sets before applying the equilibrium constraint.

(a)	(b)	(c)	(d)
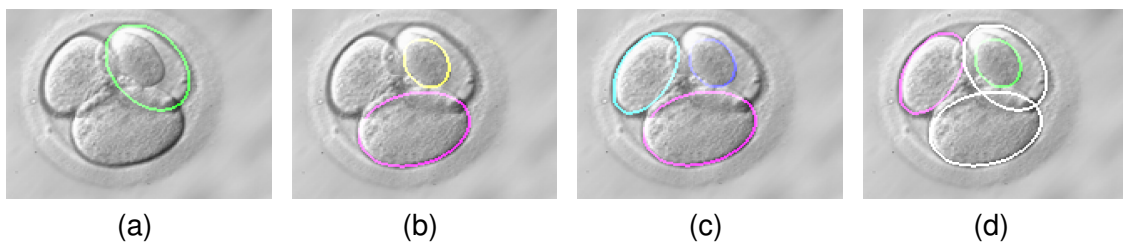
Figure 2.18: Hypotheses sets with cardinality of 1 to 4.

As the embryo images contains a maximum of four blastomeres, the ellipsoids are grouped into sets of 2 to 4 cell equilibriums. The sets with centroids that are less than 10 pixels away from the centroid of the embryo are retained, while others are removed as outliers. This further reduces the blastomeric candidates, as shown in Fig. 2.19(a). In this case, one blastomere is fully fallen behind another and therefore are removed, Fig. 2.19(b). The accuracy of the ellipse modeling on blastomeres is computed using the intersection of the obtained results with those of the manually identified ground truth as shown in Fig. 2.19(c).

(a) (b) (c)
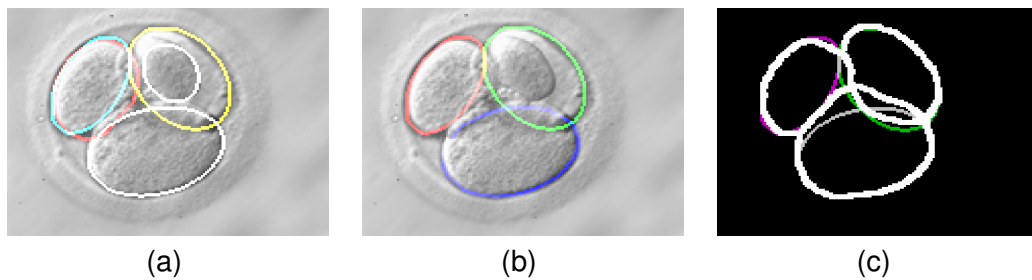
Figure 2.19: Blastomeres: (a) satisfying the equilibrium, (b) after removal of contained candidates. (c) Final results are displayed on the top of ground truth.

2.4 Parameters, Experimentation and Results

The proposed algorithm is tested on a dataset of 40 HMC embryo images with ten images for each of the one, two, three and four blastomere embryos. Blastomere extraction is a difficult problem due to fragmentation, uneven size of blastomeres and occlusion between neighbouring blastomeres. The algorithm is applied for blastomere extraction using a single set of parameters for all images. Qualitative and quantitative evaluations, comparisons with other methods, as well as performance aspects in terms of implementation and portability are presented next.

2.4.1 System Parameter Settings

The proposed system has a few parameters that are set according to the characteristics of the input images. In this section, we explain the reason behind the values selected for such parameters as this knowledge might help to port our system for input images of different

sources. We consider these parameters to be the most important ones in the success of our algorithm for other images.

2.4.1.1 Isoperimetric partitoning

Isoperimetric algorithm is utilized to segment the input image into regions corresponding to blastomeres as shown in Fig. 2.15(b). The algorithm differentiates the foreground from the background based on the value of α (0.6 for this work) as mention in Section 2.1.1.4. In order to select the optimal value of alpha (α), isoperimetric partitioning is applied on training images with different alpha values. In each case, the alpha value that segments an embryo image into regions that closely resemblance blastomere cells in the image, is selected. The final alpha value is computed by taking the average of all alpha values corresponding to each training image. Furthermore, isoperimetric partitioning is a recursive process and the process is continued for each segment until the isoperimetric constant value of all partitions becomes smaller than a stop value of 0.05 taken from the original work mentioned in [26].

2.4.1.2 Region Merging Algorithm

Region merging algorithm is used to merge regions generated by isoperimetric segmentation that don't correspond to a real blastomere. The algorithm uses the length, the entropy, and the vesselness of each partition as well as its area to merge unwanted regions formulated in Equation. 2.17. All partitions that are below a merging threshold are removed resulting into merging of unwanted regions as explained in Section 2.1.2. In order to compute a proper value of the merging threshold that somehow fits all of our input images empirically, the merging algorithm was applied to a 10 embryo images. In each case, the value of the merging threshold was adjusted such that all the false partitions that don't correspond to a real blastomere are merged. The estimated weights corresponding to length, entropy and vesslness along with the *merging threshold* are presented in Table. 2.2.

Table 2.2: Empirically estimated mean threshold and weights used in Region Merging algorithm.

Merging Threshold	W_1 (Length)	W_2 (Vesselness)	W_3 (Entropy)
0.8	0.5	0.3	0.2

2.4.1.3 Ellipsoid Fitting
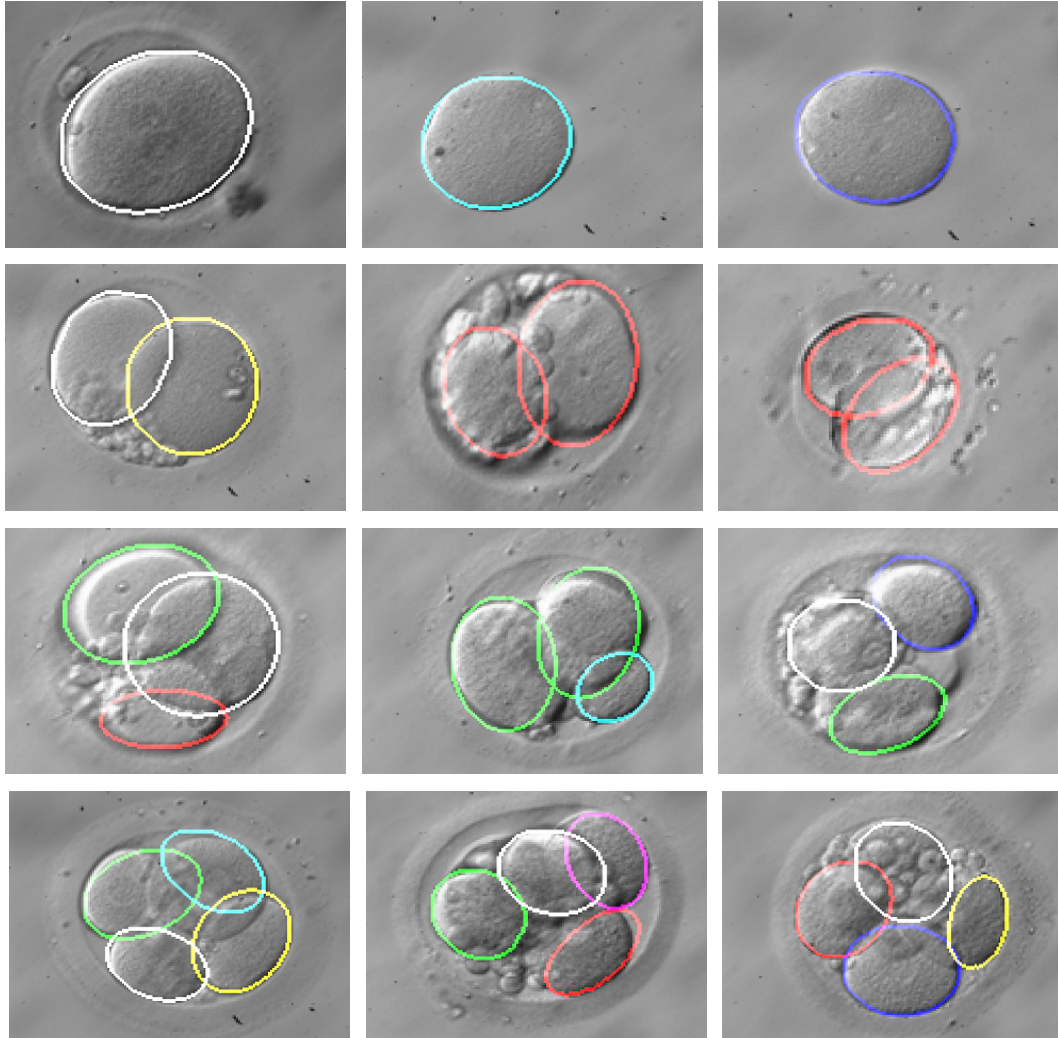
Figure 2.20: Sample results for the proposed algorithm. Each row represents input images with a certain number (1 to 4) of cells.

Ellipsoids generated from the edge image are fitted on the reduced partition set to find the ellipses that best correspond to the segmented regions as explained in Section. 2.13. Edges of the input image are computed by first smoothing the image using anisotropic diffusion [33] and then applying a Hessian based edge detector [34]. A least-squared ellipse fitting algorithm [35] is further used to produce a set of candidate ellipses for each pair of edges. The parameters used by the above three methods are presented here:

1. *Anisotropic diffusion*: Anisotropic diffusion is used to reduce noise in embryo images without blurring the edges of blastomeres as mentioned in Section. 2.1.3. Diffusion with an integration constant of 0.3 and a gradient modulus threshold of 30 was applied to all the images presented in this work.

2. *Hessian based edge detector*: We used a Hessian-based edge operator to generate the edge model for our embryo images. The operator filters each image using a 5 $\times$ 5 Gaussian kernel with a standard deviation of 10 pixels before extracting the edges.

3. *Least-squared ellipse fitting*: Least-squared ellipse fitting is used to fit ellipsoids shapes on the reduced region set obtained after region merging. The fitting algorithm fits ellipsoids with a maximum error tolerance of 10^{-5} and a maximum of 200 iterations for the Gauss-Newton step for all the regions in the reduced region set.

2.4.1.4   Set Based Candidate Selection

Set based candidate selection chooses the best ellipse for each region and places them in a reduced region set from the total ellipse candidates using the least squared error minimization method. The algorithm uses the following measures to eliminate less probable ellipse candidates:

1. *Large candidate removal*: Large ellipsoids in the candidate set are less likely to be a best fit for any region as explained in Section. 2.1.4.1. Hence, ellipsoids which occupy more than 70% of the embryo area are removed.

2. *Similar candidate removal*: The ellipsoid set may contain multiple candidates that are very similar in shape, size, or spatial location. Ellipse candidates with a similarity index more than 95% are eliminated from the candidate set.

3. *Contained and Disjoint*: According to the characteristics of embryos with two to four blastomeres, the blastomeres never contain other blastomeres within an embryo image. Utilizing these properties, an ellipse candidate having more than 90% overlap with another candidate is removed from the candidate set. In addition, disjoint blastomeres are never present within an embryo image. Based on the disjoint property of blastomeres, the ellipse candidates with no area overlap are also eliminated from the candidate set.
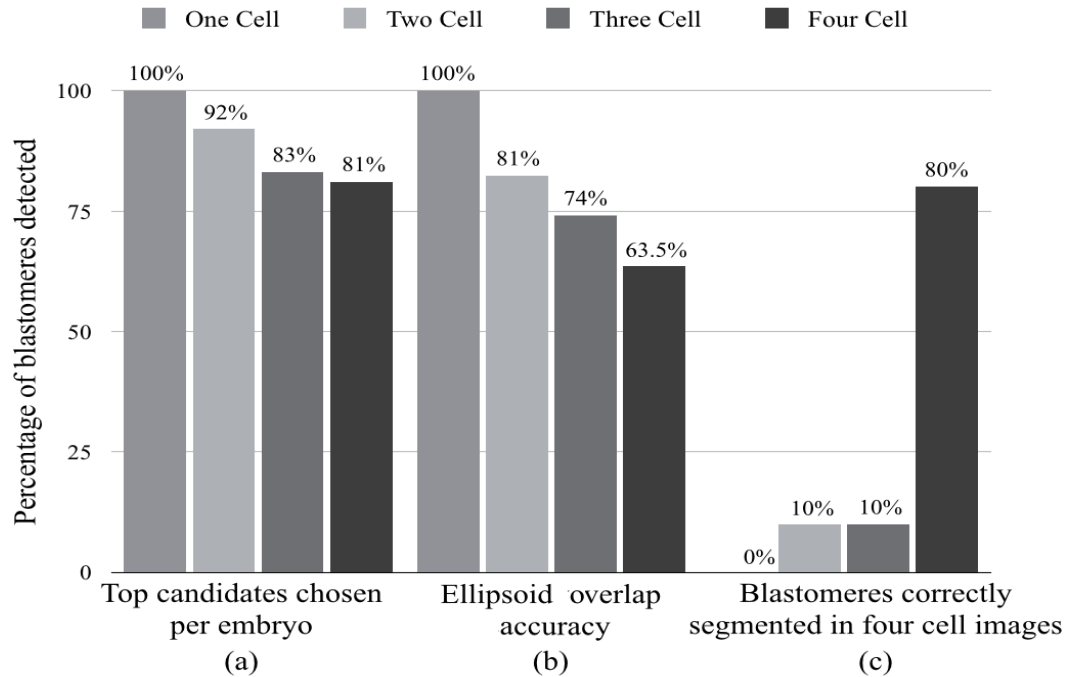
Figure 2.21: (a) Percentage of blastomeres detected in each category. (b) Accuracy of the models fitted to the blastomeres in each category. (c) Percentage of blastomere candidates correctly segmented in all four-cell embryo images.

2.4.2   Qualitative Evaluation

In this section, we present some typical results for our proposed algorithm as shown in Fig. 2.20. The results presented in Fig. 2.20 show that the algorithm can accurately extract the blastomeres in the cases of one and two cell images. However, with increase in number of blastomeres, the algorithm under-fits and over-fits ellipsoids to blastomeres due to the factors mentioned in Section. 2.1.2. Hence, the algorithm is not able to perfectly extract the blastomeres in embryo images with more than two cells.

2.4.3   Quantitative Evaluation

Quantitative evaluation of the results demonstrate the performance of the proposed algorithm based on three measures: (i) Identification of blastomeres (ii) Identification of the shape of the blastomeres, and (iii) Comparison with state of the art. Fig. 2.21(a) visualizes the accuracy of the proposed detector in identifying blastomeres within an embryo image containing different number of cells. All blastomeres in 10 one-cell embryo images were

identified correctly resulting in 100% accuracy. Unfortunately, the results for the images of 2, 3 and 4 cells are less accurate. The second performance measures the accuracy of the detector based on the shape of the blastomeres. The shape accuracy obtained by finding the overlap between the true boundaries of blastomeres and those found by our algorithm, presented in Fig. 2.21(b). Finally, the proposed algorithm is compared with the state of the art algorithm proposed by Giusti *et al.* [21]. The proposed algorithm is compared with Giusti's method by measuring the number of blastomeres identified by both algorithm within a four cell embryo image. Currently, the only reported work in this area is by Giusti *et al.* [21], which has an accuracy of 71%. Our proposed algorithm is capable of identification and modeling of blastomeres in HMC images of human embryos with an average accuracy of 80% with a standard deviation of 10.03%. As observed from the graphs, single cells are easier to segment comparing to four or more cells due to the fact that there are more overlaps between the blastomeres that seem to make the task harder in these cases.
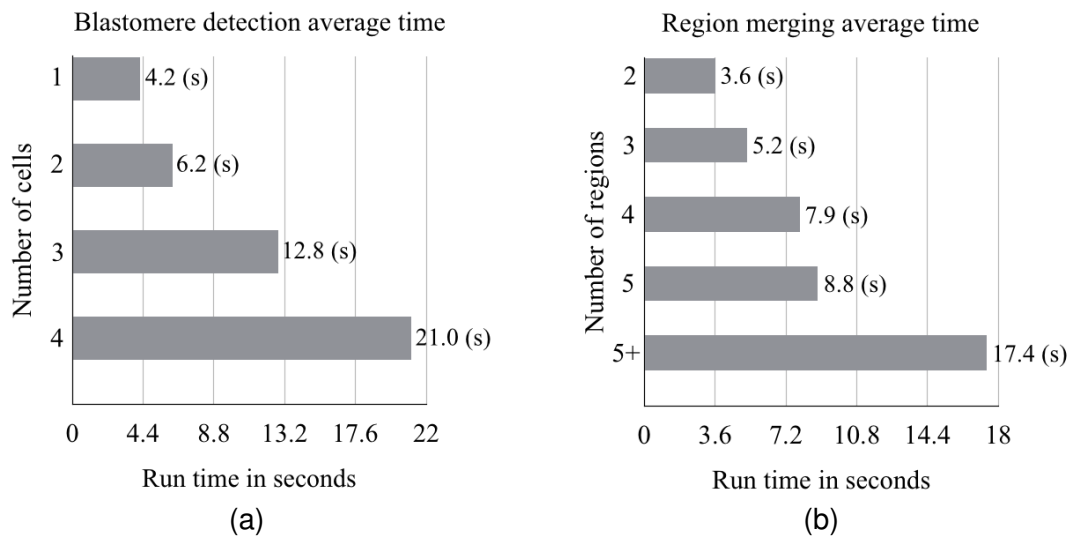
Figure 2.22: Average running time for (a) blastomere detection for each category, (b) region merging for different number of regions.

2.4.4 Performance

The proposed system is implemented in Matlab 7 and tested on a PC (CPU Intel Core2 Quad 2.26 GHz with 2 GB RAM). The input images are 620×500 pixels. The entire extraction process takes an average of 4.2, 6.2, 12.8 and 21.0 seconds to complete for

one, two, three and four cell embryo images, respectively as shown in Fig. 2.22(a). Due to the complexity of images with more blastomeres, the average time for segmenting such images is higher than the ones with lower number. The average time for segmenting blastomeres as a function of number of partitioned regions is also presented for each category in Fig. 2.22(b).

Chapter 3

Trophectoderm Segmentation

3.1 Introduction

Accurate assessment of embryos viability is an extremely important task in the optimiza-
tion of IVF treatment outcome. One of the common ways of assessing the quality of a
human embryo is grading it on its fifth day of development based on morphological quality
of its three main components: Trophectoderm (TE), Inner Cell Mass (ICM), and the level
of expansion or the thickness of its Zona Pellucida (ZP). In this work, we propose a fully
automatic method for segmentation of TE region of blastocysts (day five human embryos).
Researchers are continuously making efforts towards developing techniques and measures
that enhance the chance of selecting viable embryos. These efforts have led to the devel-
opment of grading systems that are used to bench mark embryos into different categories
according to their potentials in leading to live birth. A morphological grading system crafted
by Gardner and Schoolcraft [37] is widely adopted by IVF clinics for selecting the embryo
with the highest quality based on three morphological measures [38]. Despite the availabil-
ity of such scoring metric, it is very difficult to choose one embryo over its siblings without
knowing the relative contribution of each parameter. Experiments by Ahlstrom *et al.* [39]
has shown the superiority of grading TE over other measures, which can be further used
to select the embryo(s) with the highest implantation potential from a group of embryos.
The study also presented an essential need for a strong TE layer for successful hatching of
an implanted embryo. Hence, it is extremely important and necessary to analyze the TE's
quality to assess the quality of an embryo at the blastocyst stage.

In the past, medical professionals have manually analyzed human embryos and further guessed the probability of live birth associated with such embryos. Bendus *et al.* [40] proved that the involvement of human embryologists may lead to significant differences between the scores allocated to a set of embryos by different embryologists. It is impossible to avoid such difference in these scores resulting in a direct impact on the likelihood of IVF success. This difference can potentially be avoided by taking aid from automatic methods that are capable of computing more robust and precise scores.

A number of attempts have been made in the past to analyze human embryos using semi-automatic techniques. Hnida *et al.* [41] presented a semi-automatic software to analyze human embryo's morphology. FertiMorph, a semi-automatic system by IHMedical A/S, Copenhagen, Denmark, was proposed for analyzing the blastocyst size in a sequence of embryo images. They used variational level set algorithm proposed by Li *et al.* [42] to segment the TE's inner boundaries.

Although some semi-automatic methods have been developed in the past, full automaton has yet not been achieved due to the complex nature of patterns and shape of different components of an embryo at different stages. In addition, a significant error can occur in automatic identification due to the image quality and debris in the neighborhood of an embryo's growing environment. In this paper, we propose a robust and automatic segmentation method for TE that performs accurately even in the presence pf partial views of other embryos and occasional debris in the blastocyst background. We utilize the Retinex algorithm [43] to de-emphasize cells in the cavity area and further apply a level set algorithm [44] to segment TE regions in the blastocyst image. The superiority of our algorithm over previous work is demonstrated using blastocyst images of all TE grades.

The chapter is divided into the following sections. Section 3.2 describes the blastocyst grading system. The previous work in computer-based embryo image processing and analysis is also presented in that section. Section 3.3 explains details of the proposed segmentation algorithm. Section 3.4 overviews our image acquisition device and its settings as used for capturing our dataset images. Section 3.5 describes the ground truth establishment. Finally, Section 3.6 details related parameters and the experimental results on our database of HMC embryo images. It also provides performance related details.

3.2 Blastocyst Grading

Before providing more details of the proposed method, it is essential to develop an understanding of blastocyst components and grading. Each blastocyst consists of cavity that is filled with fluid enveloped by single layer of cells known as Trophectoderm (TE). In addition to TE, the cavity contains a set of cells known as the Inner Cell Mass (ICM) that is responsible for the formation of definitive structures of the fetus. Each embryo has a glycoprotein membrane surrounding the cells inside of the embryo named Zona Pellucida (ZP). The ZP membrane helps maintain the proximity of the blastomeres before compaction which occurs after day 3 of development. The image of a human blastocyst with its different components is displayed in Fig. 3.1.
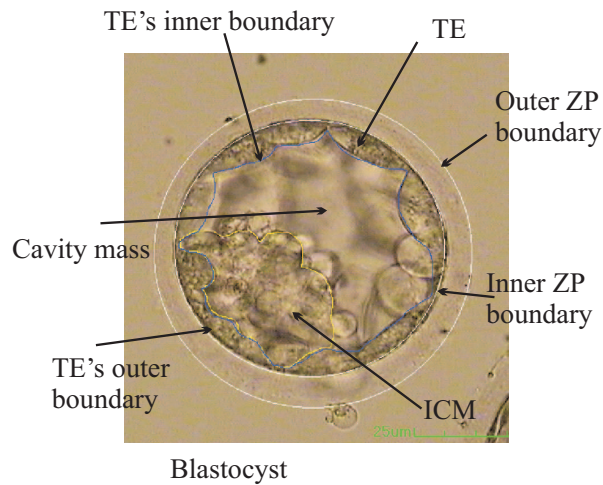
Figure 3.1: Human embryo on day 5 (blastocyst stage) of its creation.

Gardner's grading system [8] ranks blastocysts from 1 to 6 for development, A or B or C for ICM's quality, and A or B or C for TE's quality. Since the objective of the proposed work in this paper is only to segment TE region, we only describe the TE quality measures. TE quality of A represents many cells in a unified tightly packed layer, B denotes few cells in a loose-fitted epithelium, and C characterizes a collection of few large cells. Fig. 3.2 depicts three images of a blastocyst with different TE grades.

Currently, the decision on which embryo to transfer is made on the basis of morphological assessments of embryos conducted by embryologists and endocrinologists in the IVF
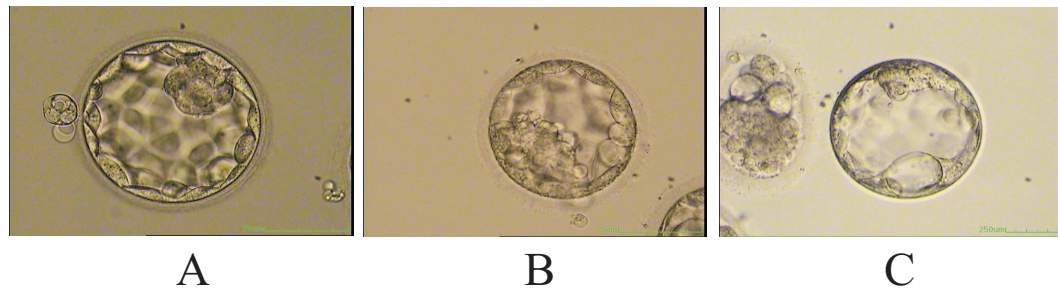
Figure 3.2: Sample images of three grades of TE (A to C).

laboratories [8],[45],[46]. There are a number of morphological features that have shown some association with embryo viability, but it is not always clear how these features should be weighted relative to one another. Moreover, the available grading systems mostly rely on the visual information that are observed by embryologists and therefore are subjective and highly dependent on the level of expertise and experience of the observers (and to some extent intra-observer) [40]. Automated image analysis could add objectivity to the processes of embryo assessment and selection, and consequently lead to better identification of viable embryos.

3.2.1   Previous Work in Computer Based Embryo Analysis

Much of the clinical research in IVF is focused on analyzing different aspects of an embryo while under development and ultimately grading it according to its morphology, size and shape at different stages of growth, fragmentation, development rate etc. Most aspects of such analysis, however, are performed manually. While there are some user interface and software tools that could assist researchers to perform region and boundary identification as well as computing various measures, there are very few machine-vision based systems that could perform any of the above tasks automatically.

A number of previous works (although not that many) have been presented for identification and grading of different components of human embryos in Hoffman Modulation Contrast (HMC) microscope images. Pedersen and Olsen [20] used level sets by Zhao-Chan [47], to model embryos' boundaries. Karlsson *et al.* [48] described an automatic area-based segmentation system for identification of the inner and outer circumferences

of ZPs with 88% success rate using 48 samples. Morales *et al.* [49] presented a system using Canny edge detection [50] and active contours to highlight ZP contours. Filho and Noble [51] presented a semi-automatic blastocyst grading system. They utilized training sets to establish fundamental characteristics of class centeroids and then they classified each region according to its distance from classes' centers using support vector machines (SVM). The feature vectors that represented each embryo were composed of a set of moments calculated based on the embryo image histogram. They identified the outer and inner boundaries of TE regions and computed the fractal dimension correlating with the number of TE cells.

As presented in the above reviews automatic analysis of embryo images has not yet attracted much attention from the image analysis and computer vision community and only very few researchers have reported their work on this field. The potential for making a contribution in this area is significant. In this chapter, we propose a novel method that automatically identifies TE regions. We extend on the preliminary work reported by Santos Filho *et al.* [51] through presenting a full feature extraction procedure. We present the pre-clinical results of our approach and suggest some potential avenues of future work.

The main contribution of this work is in introducing a fully automatic machine based system for identification of TE regions in images of human embryo blastocysts. The system requires no manual pre- or post-processing of the input images.

3.3   Proposed Method

The segmentation algorithm proposed in this work comprises of three main components. The first component is the Retinex algorithm that is used to smoothen the cavity area of the embryo. The second component of the algorithm is the level-set algorithm used to segment the TE regions. The third and final step of the algorithm is a post-processing procedure that is aimed for final cleaning and segmentation. Fig. 3.3 displays the block diagram of the proposed method. Details of each section is described next.

3.3.1   Retinex Theory

The 2D projection of a 3D spherical embryo, the transparency of the embryos's shell, and the focus/fixation of the imaging device could create visual artifacts that appear as shadows
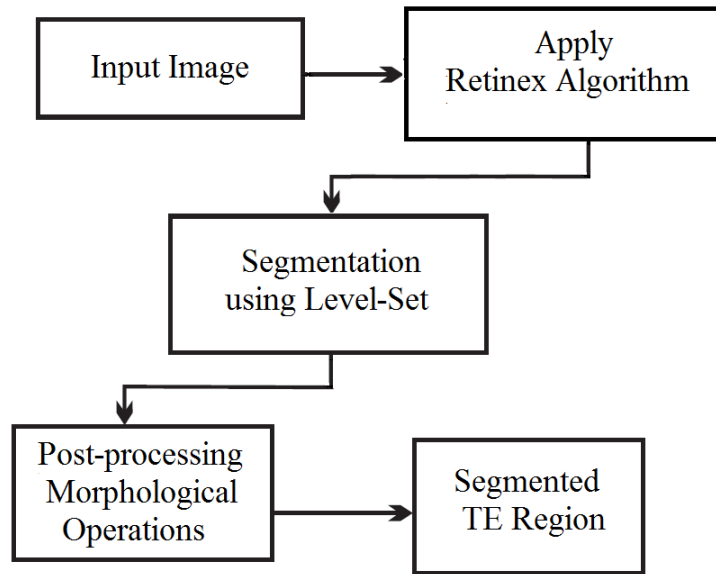
Figure 3.3: Proposed system flowchart for segmentation of TE regions.

and ghost like cells on the cavity regions of blastocyst images. The image data in the cavity region includes low frequency components with small slopes that are similar to those of non-uniform illumination.

In order to remove these low frequency components, we make use of Retinex algorithm [52]. This algorithm exploits the property of human visual system to achieve color constancy by reducing the impact of the illumination component on the reflectance component of an image. Retinex is also utilized for digital image enhancement and lightness/color rendition [53].

According to this theory, the observed color/intensity of an object depends on the light reflection property of the object and not the absolute value of the intensity of the light source. Therefore, by computing the ratio of light and shade in an image, one may correct the gray scale values of the image in shaded areas. The Retinex algorithm has been modified and presented in many different ways for various applications with different efficiencies [54–56]. The first group of Retinex algorithms were of random walk type [52]. They compute the relative relationship between light and shade by walking along all 1D

paths in the entire image and computing reflection values (at each pixel) that depend on the average value of the light to shadow ratio of all pixels in a global scale. The second group of Retinex algorithm [55, 56] use Homomorphic filtering [57]. They utilize the fact that illumination in an image is expected to be spatially smooth while the sharp details are associated with the reflectance. The third group of Retinex algorithm are based on an iterative spatial comparison of the image pixels to gradually adjust the maximum brightness [58, 59]. The fourth group of Retinex algorithms focus on improving the efficiency of the algorithm [43, 60]. Through different assumptions these methods make the Retinex algorithm a candidate for Poisson formulation. For this, often the image Laplacian and a thresholding method are utilized to highlight or extract image discontinuities.

In this work we have adopted the Retinex algorithm proposed by Morel *et al.* [43]. On an image, paths are defined by a set of pixels starting from a pixel x and ending at a random stopping pixel y [52]. At image boundaries, these random paths approximate Brownian paths. Isotropic Brownian paths are function of radial distance from a pixel coordinate and hold similar values in all directions subject to the same parameter settings and similar gradient slopes in the image plane.

We further adopt the formulation of discrete random walks over an image grid from [61]. This formulation considers a collection of N walks or paths $1, \cdots, k, \cdots N$, starting at x_t and ending at an arbitrary pixel y. n_k denotes the number of pixels of the path k, and x_i and x_{i+1} ($i = \{1, ...n_{k-1}\}$) represent two consecutive points in the path k. All these paths for the collection of N walks that are formulated on an image I of $M \times N$ pixels are defined on the discrete rectangular grid R, with x_t as the starting pixel and y as ending pixel. The Neumann boundary condition [62] is forced by converting the image into a symmetric and periodic image of size $2M \times 2N$ pixels by first mirroring the image across its right, and then bottom sides. Morel *et al.* [43] considers a target pixel y is met when the random walk from x_t and $\hat{x}_t$ both stop at y. Here $\hat{x}_t$ is conjugate to x_t in the image plane which is both symmetric and periodic. The random walk is expected to stop in finite-bounded time $n(y)$. The symmetric random walk is hence defined as:

$$x_t^y = \begin{cases} x_t & \text{if } t <= n(y) \\ y & \text{otherwise} \end{cases} \tag{3.1}$$

The relative lightness of a random walk starting at x and stopping at y is defined as:

$$L(x; y) = E \sum_{t=1}^{n(y)} \delta \left(log \left(\frac{I(x_t^y)}{I(x_{t+1}^y)} \right) \right) \tag{3.2}$$

here E is the expectation or the average over all the paths in the image plane. For a fixed contrast threshold t, δ is defined by:

$$\delta(s) = \begin{cases} s & |s| \geq t \\ 0 & |s| < t \end{cases} \tag{3.3}$$

Equation 3.3 represents that if the log difference of pixel values between adjacent pixels is less than a predefined threshold (t), one may perceive no change in the lightness of those pixels. In case the of Retinex algorithm, the definition of lightness holds for a standard random walk. The relative lightness $L(x, y)$ in a chromatic channel is the unique solution to the Poission's equation with the Neumann boundary condition given by:

$$\begin{cases} -\Delta_x L(x, y) = F(x) & \text{if } x \neq y, x\epsilon R \\ \frac{\partial L}{\partial n} = 0 & \text{if } x = \partial R \end{cases} \tag{3.4}$$

here Δ_x is defined as the Laplacian operator with respect to x and $F(x)$ is defined as:

$$\begin{aligned} F(x) = & v \left(\frac{I(x)}{I(x_{-0})} \right) + v \left(\frac{I(x)}{I(x_{+0})} \right) + \\ & v \left(\frac{I(x)}{I(x_{0-})} \right) + v \left(\frac{I(x)}{I(x_{0+})} \right) \end{aligned} \tag{3.5}$$

and

$$v(x) = \delta(log(x)) \tag{3.6}$$

The above equation is identical to Poisson's equation as formulated by Perez *et al.* [62]. Here the main objective is to remove the gradient of lightness on the left side for first condition of the Equation 3.4, which are less than a specified threshold t. In order to evaluate the derivative of $L(i, j)$, it is essential for us to solve the function $F(i, j)$ using the discrete Laplace operator on the image plane defined as:

$$\Delta v(i,j) = v(i+1,j) + v(i-1,j) + v(i,j+1)+$$
$$v(i,j-1) - 4v(i,j) \tag{3.7}$$

here (i,j) represent the coordinates of a pixel point in the image domain R. The small gradients of the image are eliminated using Equation 3.3.

The lightness value in the frequency domain can be obtained more efficiently by solving the the Poisson equation in the Fourier space using the discrete Fourier transform:

$$-\hat{L}(k,l) = \frac{\hat{F}(k,l)}{\left(4 - 2cos\frac{2\pi k}{N} - 2cos\frac{2\pi l}{N}\right)}, \quad \text{for}(k,l) \neq (0,0) \tag{3.8}$$

The lightness values are then converted back to the discrete image domain R using inverse discrete Fourier transform. The lightness value for each point on the grid is normalized to a band of [0-255].

As mentioned earlier, the main purpose of the Retinex algorithm in our system is to smooth the cavity region in blastocyst images. The main characteristic of the cavity is that it includes more low frequency components comparing to the TE or ICM regions. Such pre-processing leads to a better performance of the level set algorithm in identification of TE inner boundaries. Fig. 3.4 shows a typical blastocyst image before (a) and after (b) the application of Retinex algorithm.

(a)   (b)
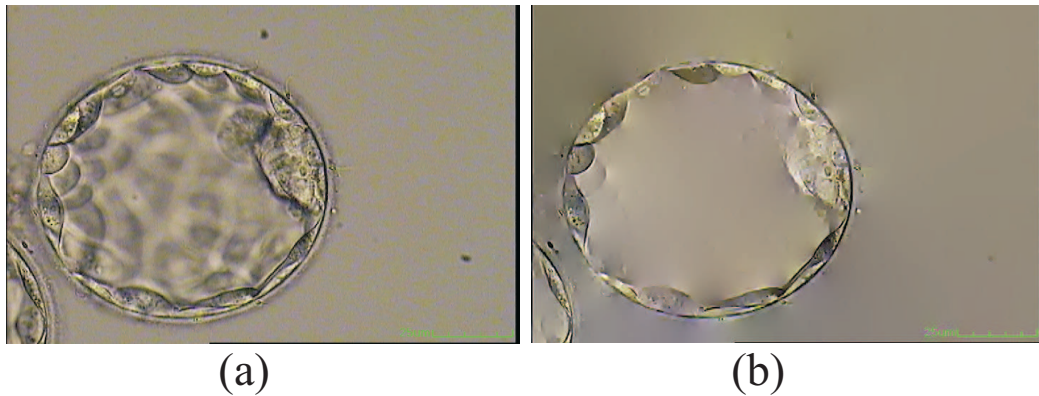
Figure 3.4: (a) Input blastocyst image. (b) Blastocyst image after the application of Retinex.
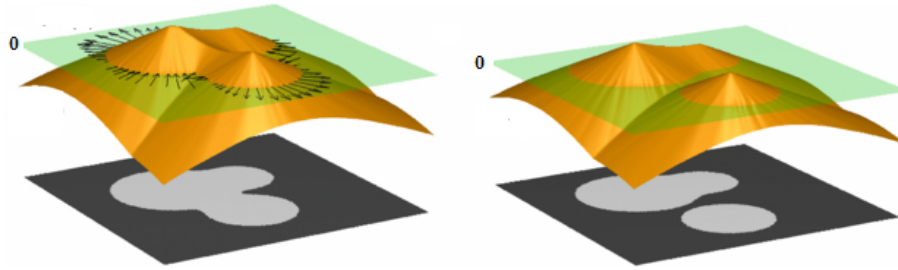
Figure 3.5: (a) Illustration of a circle embedded within a cone. (b) Illustration of how one closed contour embedded in a surface is related to two closed contours on another level.

3.3.2 Level-Set Background

In image processing and computer vision applications, the level-set method was introduced independently by Caselles *et al.* [63] and Malladi *et al.* [64] in the context of active contour (or snake) models [65] for image segmentation. To distinguish it from Snakes, it is sometime called implicit (vs. explicit for Snakes) or geometrical (vs. parametrical) Active Contour Models. The segmentation problem reduces to finding curve(s) to enclose regions of interest. Intuitively, we can model the curves directly using control points.

The idea behind the level-set method is to imbed a curve within a surface. In our case, we imbed a two-dimensional curve within a three-dimensional surface. To illustrate this point, Fig. 3.5(a) shows how a circle can be imbedded into a cone. By indirectly modelling curves, the above mentioned problems of splitting and merging curves are addressed without the need to treat them as special cases. Fig. 3.5(b) shows how a curve can split into two by moving along the surface of the level-set. Using this idea, we can morph the surface to achieve our desired topology at a specific contour level.

3.3.2.1 Level-Set Formulation

Early active contour models are formulated in terms of a dynamic parametric contour $c(s,t) : [0,1] \times [0,\infty) \rightarrow R^2$ with a spatial parameter in [0,1], which parameterizes the points in the contour, and a temporal variable . The curve evolution can be expressed as

$$\frac{\partial C}{\partial t} = FN \tag{3.9}$$

where F is the speed function that controls the motion of the contour, and N is the inward normal vector to the curve C. The curve evolution in Equation 3.9 in terms of a parameterized contour can be converted to a level-set formulation by embedding the dynamic contour $C(s, t)$ as the zero level set of a time dependent level-set function $\phi(x, y, t)$. Assuming that the embedding level-set function ϕ takes negative values inside the zero level contour and positive values outside, the inward normal vector can be expressed as:

$$N = -\frac{\nabla \phi}{\nabla \phi} \tag{3.10}$$

where ∇ is the gradient operator. Then, the curve evolution Equation 3.10 is converted into the following partial differential equation (PDE):

$$\frac{\partial \phi}{\partial t} = F|\nabla \phi| \tag{3.11}$$

which is referred to as a level set evolution equation.

The equivalent in the level-set model is to choose the propagation speed term defining F. The requirements will be similar: we want to incorporate a regularization term ("internal"), a term that will encourage stopping at edges ("external") and an inflation term ("external-balloon"). To account for regularization, Malladi *et al.* [64] suggested a curvature dependant speed $F = F(k)$, for example, $F = -k$ (concave points go faster in the normal direction. To get an inflation force we add a constant term F_0:

$$F(k) = F_0 - k \tag{3.12}$$

and so we are left with the edge-stop term. The above speed term is multiplied further by function:

$$g(x, y) = \frac{1}{1 + |\nabla G_\sigma * I(x, y)|} \tag{3.13}$$

This function behaves as an inverse of a gradient operator. It therefore, approaches zero in the vicinity of an edge, bringing the velocity to a stop. Smoothing by a Gaussian filter helps skipping weak edges. Putting it all together in (2.10) we will get:

$$\frac{\partial \phi}{\partial t} + g(x,y)(F_0 - k)| \bigtriangledown \phi| = 0 \tag{3.14}$$

Incorporating the classical equation for the curvature k:

$$k = div(-\frac{\bigtriangledown \phi}{\bigtriangledown \phi}) = \frac{\phi_{yy}\phi_x^2 - \phi_x\phi_y\phi_{xy} + \phi_{xx}\phi_y^2}{(\phi_x^2 + \phi_y^2)^3/2} \tag{3.15}$$

and changing the sign F_0 (can be positive or negative), we get the final level-set flow as a PDE:

$$\frac{\partial \phi}{\partial t} = g(x,y)| \bigtriangledown \phi|(F_0 + div(-\frac{\bigtriangledown \phi}{\bigtriangledown \phi})) \tag{3.16}$$

3.3.3 Piecewise Method

Let Ω be the image domain, and $I : \Omega \to R$ be a gray level image. In [66], a segmentation of the image I is achieved by finding a contour C, which separates the image domain Ω into disjoint regions $\Omega_1, ..., \Omega_N$, and a piecewise smooth function u that approximates the image I and is smooth inside each region Ω_i. This can be formulated as a problem of minimizing the following Mumford-Shah functional:

$$F^{MS}(u,C) = \int_{\Omega}(I - u)^2\partial x + \mu \int_{\Omega \backslash C} | \bigtriangledown u|^2\partial x + \nu|C| \tag{3.17}$$

where $|C|$ is the length of the contour C. In the right hand side of Equation 3.17, the first term is the data term, which forces u to be close to the image I, and the second term is the smoothing term, which forces to be smooth within each of the regions separated by the contour C. The third term is introduced to regularize the contour C.

Let $\Omega_1, ..., \Omega_N$ be the regions in Ω separated by the contour C, i.e. $\Omega \setminus C = \cap_{i=1}^N \Omega_i$. Then, the contour C can be expressed as the union of the boundaries of the regions, denoted by $C_1, ..., C_N$, i.e. $C = \cap_{i=1}^N C_i$. Therefore, the above energy $F^{MS}(u,C)$ can be equivalently written as:

$$F^{MS}(u_1, ..., u_N, \Omega 1, ..., \Omega_N) = \sum_{i=1}^N (\int_{\Omega_i}(I - u_i)^2\partial x + \mu \int_{\Omega_i} | \bigtriangledown u_i|^2\partial x + \nu|C_i|) \tag{3.18}$$

where u_i is a smooth function defined on the region Ω_i. The methods aiming to minimize this energy are called piecewise smooth (PS) models. In [67], [68], level-set methods were proposed as piecewise smooth (PS) models for image segmentation.

The variables of the energy term F^{MS} include N different functions, $u_1, ..., u_N$. The smoothness of each function u_i in Ω_i is ensured by imposing a smoothing term $\mu \int_{\Omega_i} | \bigtriangledown u_i|^2 \partial x$ in the functional F^{MS}. To minimize this energy, N PDEs for solving the functions, associated with the corresponding smoothing terms, are introduced and have to be solved at each time step in the evolution of the contour C. This procedure is computationally expensive. Moreover, the PS model is sensitive to the initialization of the contour C or the regions $\Omega_1, ..., \Omega_N$ [66].

In a variational level set formulation [69], Chan and Vese simplified the Mumford-Shah functional to the following energy:

$$F^{CV}(\phi, c_1, c_2) = \int_{\Omega} |(I(x) - c_1)|^2 H(\phi(x)) \partial x + \int_{\Omega} |(I(x) - c_2)|^2 H(\phi(x)) \partial x + \nu \int_{\Omega} |H(\phi(x))| \partial x$$

(3.19)

where H is the Heaviside function, and ϕ is a level set function, whose zero level contour $C = \{x : \phi(x) = 0\}$ partitions the image domain Ω into two disjoint regions $\Omega_1 = \{x : \phi(x) > 0\}$ and $\Omega_1 = \{x : \phi(x) < 0\}$. The first two terms in Equation. 3.19 are the data fitting terms, while the third term, with a weight $\nu > 0$, regularizes the zero level contour. Image segmentation is therefore achieved by find the level set function ϕ and the constants c_1 and c_2 that minimize the energy F^{CV}. This model is a piecewise constant (PC) model, as it assumes that the image I can be approximated by constants c_1 and c_2 in the regions Ω_1 and Ω_2, respectively.

3.3.4 Level-Set Based Segmentation

Level-set algorithm has been widely used for identification and tracking of boundaries and shapes. In particular, level set is very good for following changes in shapes and topologies. For the purpose of blastocyst analysis, the level set by Li *et al.* [42] has been previously used by [16] in a semi-automatic manner. In this work, we aimed to utilize the level set algorithm to automatically identify TE regions as the outer and inner boundaries of TE regions seem to look distinctive. However, what we noticed was that despite the fact that

the cavity region includes low frequencies and damped edges, the level set algorithm still has difficulties in stopping at the right boundaries and often leaks into the cavity region. For this reason, we utilized the Retinex algorithm to further smooth the cavity region, as a pre-processing step, before the application of the level set algorithm for the TE region. As it is not possible to completely smooth out the cavity region, a more sophisticated level set capable of segmenting in the presence of some inhomogeneities in the form of cells is necessary. Therefore we use a new level set proposed by Li *et al.* [44], capable of segmenting in the presence of intense inhomogeneities.

In order to cope with intensity inhomogeneities in an image, Li formulated a method based on a model that considers the composition of an image as:

$$I = BJ + n \tag{3.20}$$

here J is the original or true image, B is the biased field which represents the intensity inhomogeneity and n is additive noise (zero mean Gaussian). I is an image function in image domain (Ω) defined over all real values (R). Bias Field B can be easily predicted by a neighborhood constant of each point in the image due to its slowly varying property. The true image J takes N distinct values from $c_1 \cdots c_n$ in the disjoint region $\Omega_1 \cdots \Omega_n$, respectively. Based on the assumptions stated above, our objective is to minimize the energy in a variational framework by finding the optimum regions $\{\hat{\Omega}\}_{i=1}^N$, the constants $\{\hat{c}\}_{i=1}^N$ and the estimation of bias field $\hat{B}$. Hence, the image segmentation and the bias field estimation are found simultaneously through energy minimization.

In order to compute the local intensity property, a circular neighborhood, defined by $O_y \triangleq \{x : |x - y| \leq \rho\}$ with a radius ρ centered at each point $y \in \Omega$, is considered. By assuming that the bias field is changing slowly, the value of $B(x)$ for a point x in the circular neighborhood of O_y is considered near to $B(y)$ or:

$$B(x) = B(y) \quad for \ x \in O_y \tag{3.21}$$

with the assumption that the intensities of $B(x)J(x)$ in each region $O_y \cap \Omega_i$ are close to constant $B(y)c_i$,

$$B(x)J(x) = B(y)c_i \quad for \ x \in O_y \cap \Omega_i \tag{3.22}$$

we have:

$$I(x) = B(y)c_i + n(x) \quad for \ x \in O_y \cap \Omega_i \tag{3.23}$$

Hence, the intensity in the set $(I_y^i = \{I(x) : x \in (O_y \cap \Omega_i)\})$ forms a cluster with a centroid of $m_i = B(y)c_i$, which is believed to be a sample picked out of a Gaussian distribution with a mean value of m_i. Image segmentation and bias field estimation are computed using the above formulated local intensity clustering property.

The neighborhood intensities of O_y can be classified into N clusters with centers of $m_i = B(y)c_i$ for $i = \{1 \cdots N\}$ using the clustering properties derived above. This is achieved via an iterative K-means algorithm that minimizes the clustering criteria in a continuous form [70]. Clustering criteria for classifying the intensities in O_y for a window function K is defined as:

$$\varepsilon_y = \sum_{i=1}^{N} \int_{O_y} K(y - x)|I(x) - B(y)c_i|^2 dx \tag{3.24}$$

where

$$K(u) = \begin{cases} \frac{1}{a} \exp(\frac{-|u|^2}{2\sigma^2}) & \text{for } |u| < \rho \\ 0 & \text{otherwise} \end{cases} \tag{3.25}$$

The convolution window $K(y - x)$ is constructed as a $w \times w$ mask, with $w > 4 * \sigma + 1$, defined as the Gaussian kernel in Equation 3.25. The radius ρ for the neighborhood O_y should be chosen carefully depending on the intensity inhomogeneities. For more localized intensity inhomogeneity, smaller ρ and σ should be used. The classification of local intensities depends on the minimization of the clustering criterion function ε_y. The classification is precise, if the value of ε_y is as small as possible. We need to optimize ε_y over the entire domain Ω such that ε_y is minimum for all ys in Ω. This can be realized by minimizing the integral of ε_y for all ys in image domain Ω.

$$\varepsilon \hat{=} \int \varepsilon_y dy \tag{3.26}$$

or:

$$\varepsilon \hat{=} \sum_{i=1}^{N} \int_{O_y} \left(K(y - x)|I(x) - B(y)c_i|^2 dx \right) dy \tag{3.27}$$

By minimizing the energy with respect to regions $\Omega_1 \cdots \Omega_n$, constants $c_1 \cdots c_n$ and bias

field B, segmentation can be achieved. In order to minimize the energy, the energy term is formulated in terms of the level-set function ϕ, constant vector $c = \{c_1 \cdots c_n\}$ and bias field B as:

$$\varepsilon(\phi, c, B) = \int \sum_{i=1}^{N} e_i(x)M_i(\phi(x))dx \tag{3.28}$$

where e_i defined as:

$$e_i(x) = \int K(y-x)|I(x) - B(y)c_i|^2 dy. \tag{3.29}$$

The variational level set formulation uses the energy ε as a data term as defined by:

$$T(\phi, c, B) = \varepsilon(\phi, c, B) + vL(\phi) + \mu R(\phi) \tag{3.30}$$

where the energy term $L(\phi)$ is defined as:

$$L(\phi) = \int |\nabla H(\phi)|dx \tag{3.31}$$

here H is a heavy side function, and the energy term $R(\phi)$ is defined as:

$$R_p(\phi) = \int p|\nabla \phi|dx \tag{3.32}$$

We minimize the energy $T(\phi, c, B)$ with respect to each of its variables (ϕ, c, and B) in each iteration. The result of the energy minimization for each variable is as follows:

- **Energy Minimization with respect to ϕ:**

  The energy is minimized with respect to ϕ by keeping c and B constant. After minimization the final gradient flow $\partial T/\partial \phi$ is expressed as:

$$\frac{\partial T}{\partial \phi} = -\delta(\phi)(e_1 - e_2) + v\delta(\phi)div\left(\frac{\nabla(\phi)}{|\nabla(\phi)|}\right)$$
$$+\mu div\left(d_p(|\nabla(\phi)|\nabla(\phi))\right) \tag{3.33}$$

  where ∇ is the gradient operator, div is the divergence operator and d_p is defined as:

$$d_p(s) \hat{=} \frac{p}{s} \tag{3.34}$$

- **Energy Minimization with respect to c:**

  formulation is stated as below for a constant ϕ and B. Most favorable c vector, $\hat{c} = \{\hat{c}_1, \cdots, \hat{c}_N\}$, which minimizes the energy is given by:

  $$\hat{c} = \frac{\int (B * K) I u_i dy}{\int ((B^2 * K)) u_i dy} \quad i = 1, B, N \tag{3.35}$$

- **Energy Minimization with respect to B:**

  For fixed ϕ and c, the formulation is stated as:

  $$\hat{B} = \frac{(I J^{(1)}) * K}{J^{(2)} * K} \tag{3.36}$$

  In the above equation, $J^{(1)} = \sum_{i=1}^{N} c_i u_i$ and $J^{(2)} = \sum_{i=1}^{N} c_i{}^2 u_i$. In the case of $N > 2$ or multiphase level set formulation, one may use more than two level set functions to formulate the energy function. In this application, however, we utilize a value of 2 for N as our clustering algorithm will cluster the image into two regions (TE and none TE).

Fig. 3.6 represents the output of the level set algorithm in cyan over-imposed on the smoothed version of the input image.
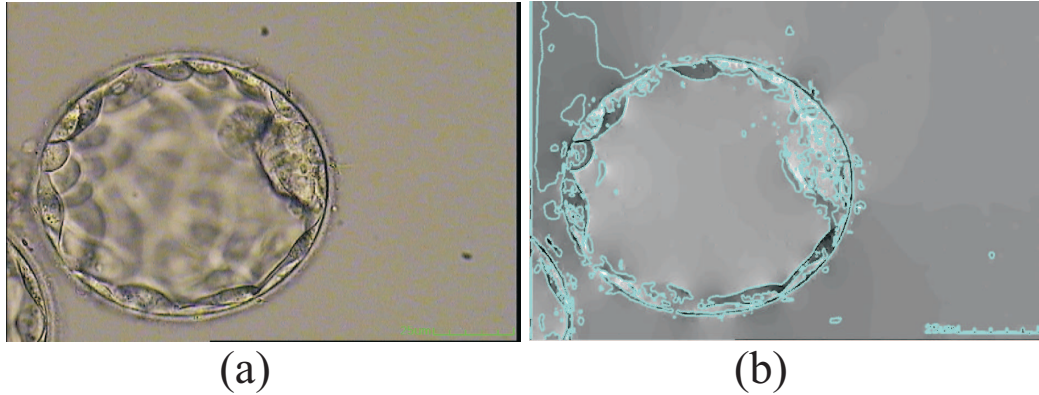

(a)   (b)

Figure 3.6: (a) Input blastocyst image. (b) Output of the level set algorithm.

3.3.5 Post-processing of Level Set Output

In this section, we perform a post-processing step to clean up and better represent the output of the level set algorithm. This is a necessary step as the output of the level set algorithm correspond to TE regions and other regions including ICM, floating cells outside the blastocysts, and some debris. Our main goal here is to precisely identify and modify those segments that correspond to the TE regions while removing those segments that correspond to others.

Here, we start with the Canny edge detector [50] that is applied on the output of the level set algorithm. Naturally, the edge detection in here will identify the boundaries of the segments identified by the level set. The resultant binary output contains a set of edges that correspond to TE segment boundaries and those of other regions. These edges may contain discontinuities that sometimes originate from TE regions with lower qualities, natural discontinuities that may exist at the outer boundaries of the TE region, and perhaps the non-customized parameter setting of the Canny edge detector. It should be noted that for all the processed images that are presented in this work, only one set of parameters is utilized for the Canny operator. These parameters include a lower threshold of 0.12 and a higher threshold of 0.3 that are found empirically.

Next, the discontinuities within or in-between the TE segments are padded using a morphological dilation operation that expands the TE segments by a structuring element of disk shape with a radius 3 pixels. The discontinuities within a TE segments (holes) and in-between the majority of TE segments are filled out after the dilation operation. However, this process is unable to fill those discontinuities in-between TE segments at larger proximity. Usually for TEs with lower qualities, it is observed that the number of disconnected TE segments is larger. In order to identify those segments that truly correspond to the TE region, we first find the center of gravity of the blastocyst mass. Here, we take advantage of the spherical shape and the circular 2D footprint of an embryo which indicate that the exterior points of the TE (which are also located on the inner ZP) have similar distances from the centroid of the embryo.

We find the center of gravity for all the segments found by the level set algorithm. This center might be a bit off from the real centroid of the embryo especially in images with debris and parts from other cells. We then radiate 72 beams with a separation of 5 degrees from the center of the mass towards outside. These beams intersect with the boundaries of

the TE regions as they move outwards. Indeed, the first and last intersections of the beams with the level set segments are recorded. We expect the second intersection of the beams to be right on the inner boundary of the ZP (also on outer boundary of the TE region) and therefore should have smooth variation comparing to the neighboring intersections. We use this property and identify those points where the intersection deviates more than ± 5 pixels from the median of the neighboring second intersections. The retained segments most likely correspond to the TE segments due to their equidistant property from the center of the mass. In addition, this process removes the segments that correspond to the debris, inside or outside the cavity region. However, this process fails to remove those segments corresponding to the ICM region in cases where the ICM is connected to the TE's interior boundary.

For those beams that intersect with the ICM, the distance of the first intersection from the center of the mass is much shorter than those cases when the beams first intersection occurs at the interior boundary of the TE region. In order to identify those intersections with the ICM, we maps the pixels from the image, i.e. Cartesian system (CS) to the points in the polar system (PS). The conversion process includes the computation of the distance and the angle for each TE pixel with respect to the embryo's center using the following formulas:

$$D = \sqrt{(y - y_0)^2 + (x - x_0)^2} \tag{3.37}$$

$$A = \tan^{-1} \frac{y - y_0}{x - x_0} \times \frac{180}{\pi} \tag{3.38}$$

here D is the distance and A is the angle w.r.t to (x, y) which is a TE pixel coordinates in CS. (x_0, y_0) is the pixel coordinates of the embryo center in CS.

Further, we use a K-means clustering approach to cluster the beams into two groups according to the distance of their first intersection with the radiated beams. Between the two found clusters, the one with the smaller centroid (shorter distance from the center of the mass) most likely corresponds to the intersection of the beams with regions in which the ICM is connected to the TE region. All those intersections are replaced with the centroid location of the other cluster. Next, the image is converted back to CS from PS using the following formulas:

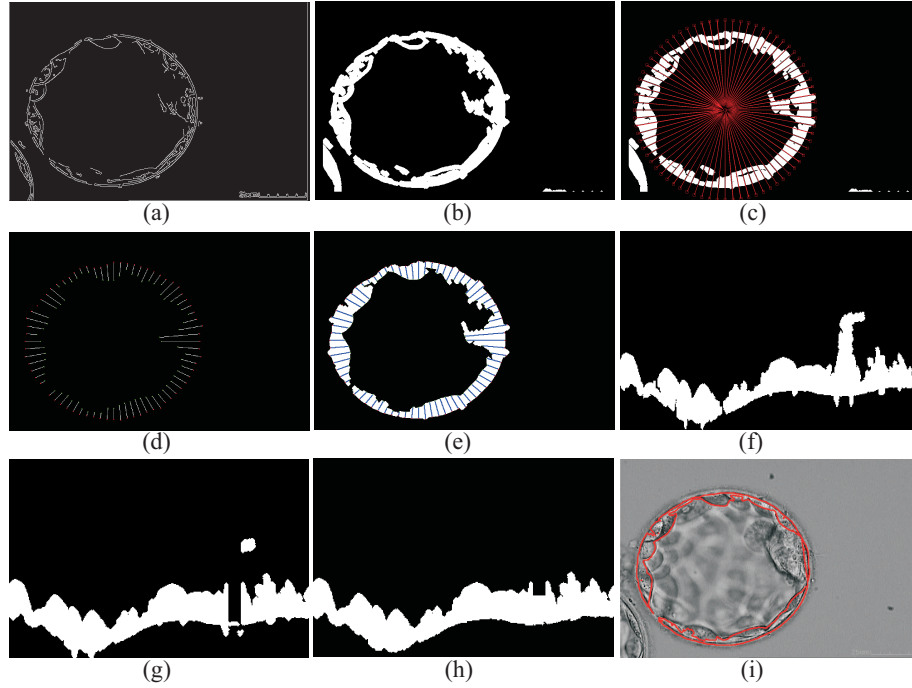$$x = D. * cosd(A) + x_0; \tag{3.39}$$

Figure 3.7: (a) Canny edge detector applied on the output of level set. (b) Canny edges are dilated. (c) Beams are radiated from the center of the mass. (d) The first and the last intersections of the segments with the beams are recorded. (e) Segments corresponding to the intersecting points are retained. (f) TE segments are converted to the polar coordinate system (CS). (g) Regions with high variation are identified and removed using K-means clustering. (h) Removed intersections are substituted with the cluster mean and are adjusted locally using level set algorithm. (i) Segments are converted back into the Cartesian CS and overlaid on the input image.

$$y = D. * sind(A) + y_0; \qquad (3.40)$$

here D is the distance and A is the angle w.r.t to (x_0, y_0) which is a TE pixel coordinates in PS and (x_0, y_0) is the pixel coordinates of the embryo's center in CS. Then, the level set is locally applied to each replaced point to allow the adjustment according to the local properties. A maximum one standard deviation from the centroid is allowed in this final adjustment.

At this point, TE segments are identified by all those regions in between the first and the second intersections with the beams. A simple erosion of one pixel is applied to remove

the exterior pixels that were added during the earlier dilation operation. Fig. 3.7 displays a visual representation of the post-processing procedure.

3.4   Image Acquisition

The blastocyst images used in the experimentation have been acquired using an Olympus IX71 inverted microscope with a Nomarski (DIC) optics. The software used for capturing our images is the Research Instrument (RI) Cronus 3. The microscope includes a built-in magnification changer of $1\times/1.6\times$; however, all the images are captured at $1.6\times$ and a lens objective of $20\times$.

3.5   Ground Truth

In order to compute the accuracy of the proposed algorithm, We have used a dataset of 100 (85 test and 15 training images) HMC human blastocyst images. These embryos were graded and their different components were manually extracted by expert embryologists: Mrs. Carole Lawrence and Mr. Jason Au, both from Pacific Center for Reproductive Medicine. We utilize the results of the manual identification as our Ground Truth (GT) or gold standard and compare the output of our algorithm with that.

3.6   Parameters, Experimentation and Results

The proposed method is tested using 85 HMC human embryo images containing embryos of grades A, B and C. These images each include one complete blastocyst with some debris or other cells in the background. Some of these images may include partial views of neighboring embryos in them. We assume that the region associated with the embryo of interest is larger than any other part in the image. A single set of parameters is used for all images. Qualitative and quantitative evaluations, comparisons with other methods, as well as performance aspects in terms of implementation and portability are presented next.
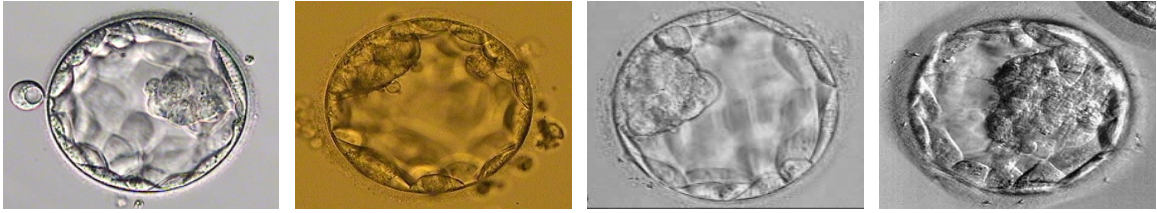
Figure 3.8: Few blastocyst images selected from the training dataset.

3.6.1 System Parameter Settings

Like any complex system, the proposed system has a few parameters that are set according to the characteristics of the input imagery. In this section, we explain the rational behind the values chosen for such parameters as we think this might help to port our system for input images from different sources. In order to customize the system for other kind of input images (captured by different groups and laboratories and perhaps with other HMC microscopes or at different settings), some of these parameters must be adjusted. We consider these parameters to be the most important ones in the success of our algorithm for other images.

3.6.1.1 Retinex

As explained earlier, the Retinex algorithm is utilized to remove small gradients inside and outside the blastocyst region, as shown in Fig. 3.4. In the Retinex algorithm, the level of smoothness of the output image depends on the value of threshold t in Equation 3.3. Clearly, this threshold must be set according to the application, and types and settings of input images. Fig. 3.9 shows a blastocyst image after application of the Retinex algorithm at three different t settings.

To find a proper value for t that somehow fits all of our input images empirically, the Retinex algorithm was applied on 15 training embryo images of different TE grades. The training dataset of 15 images was chosen from the dataset of 100 images (85 test images) such that it captures different variants of blastocyst qualities/characteristics. Few of the training images are shown in Fig. 3.8. As shown in the sample images, this dataset contains blastocyst images with different TE thickness. Also, in these images ICM appears at various locations including center and sides. This implies that in some of the images the ICM is
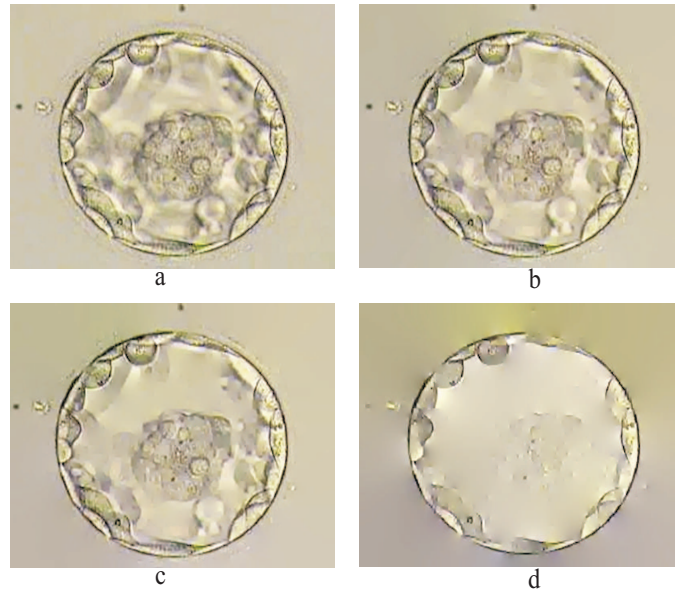
Figure 3.9: Different threshold values for Retinex algorithm: (a): Original image, (b): t=10, (c): t=20, (d): t=40.

connected to the TE layers and in some it doesn't. In each case, the value of the threshold was adjusted manually, so that the best output in terms of maximum smoothing of the cavity region was achieved. The threshold values, for all cases of different grades, as shown in Table 3.1, were averaged. The average value was then used as the parameter t whenever the Retinex algorithm was called throughout all of our experiments.

Table 3.1: Empirically estimated threshold t.

TE Grade	Mean Threshold t
A	24.3
B	26.7
C	24.4
Average	25.1

3.6.1.2 Level-set

In the succeeding step, level set algorithm is applied to the output of Retinex algorithm. The parameter N in the level set algorithm is set to 2 as we utilize the level set as a two-phase case. Parameter σ is set to 4, μ to 1.0, while $\bigtriangledown t$ to 0.1. A mask size of 17×17 pixels in accordance to the value of σ is utilized. All these values are set according to the suggestion by [44]. The value of v is set to 0.001×255^2 since our data range is $[0, 255]$.
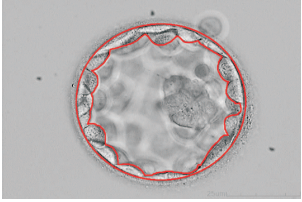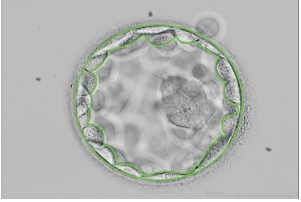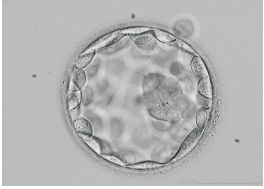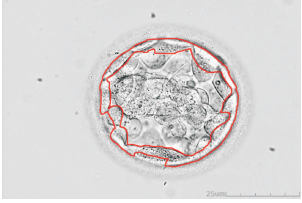
3.6.1.3 Post-processing
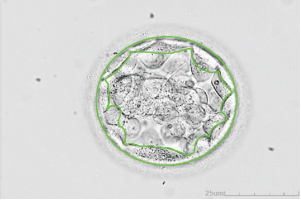
The parameters of Canny edge detector in the Post-processing Section include a lower and an upper thresholds that are set to 0.12 and 0.3, respectively. These two values are found empirically. A morphological dilation with a structuring element of disk shape (radius of 3 pixels) is then applied to the output of the Canny edge detector.
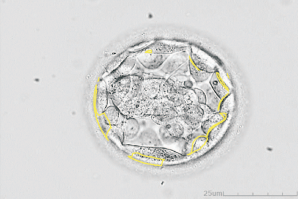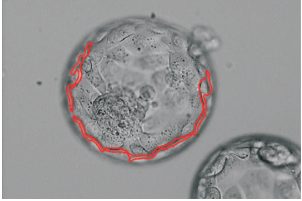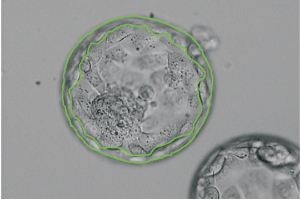
As explained in Section 3.3.5, we have used a star shape radiating beam set to choose proper segments associated with the TE region. We have used a separation of 5 degrees for those beams. A smaller value of such separation would allow catching those tiny segments that may exist in the TE region. We have not noticed significant differences in the quality of the detected TE by reducing this parameter. However, we noticed that our running time could increase slightly. Increasing this parameter, however, might cause missing few segments that ultimately might affect the accuracy slightly. We have also allowed a 5 pixel deviation in the exterior boundaries of neighboring TE segments. This value is set according to the resolution of our HMC images as well as usual offsets that may exist between the real center of a blastocyst and the center of gravity of the blastocyst mass which is used in the beam radiation process.

3.6.2 Performance

The proposed system is implemented in Matlab 7 and tested on a PC (CPU Intel Core2 Quad 2.26 GHz with 2 GB RAM). The input images are 720×479 pixels. The entire extraction process takes an average of 34 seconds to complete.
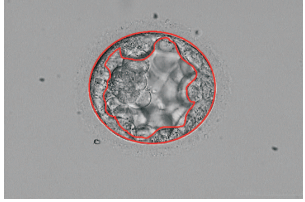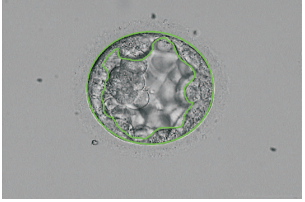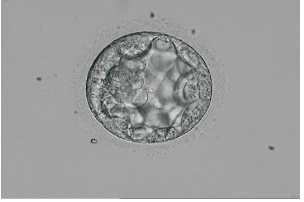
Table 3.2: Three example (best, average and worst case scenarios) outputs of the proposed algorithm along with the GT and difference between the two for sample images for grade A TEs.

Proposed Method	Ground Truth	Difference	Accuracy [%]
			100
			77.05
			27.38

3.6.3 Qualitative Evaluation

Table. 3.2, 3.3, 3.4 represents typical results for several HMC human embryo images for TE grade A, B and C with the extracted TE boundaries overlaid on the input images. The table also presents the TE ground truth boundaries extracted by the embryologist and differences between the TE boundaries extracted by the algorithm and ground truth, overlaid on the input images. To demonstrate the performance of the system clearly and with no bias, we have categorized the visual data by their grade and according to the quality of the output generated by our system. In this Table the first column represents TEs' actual grades, which were determined by our expert embryologists. The second column, Quality,
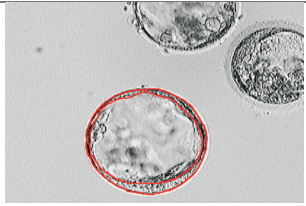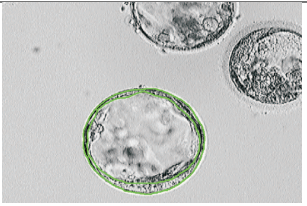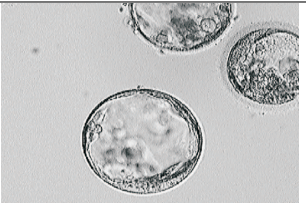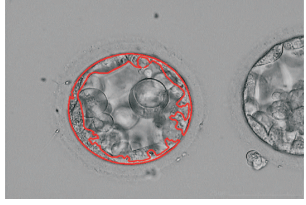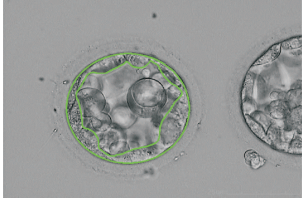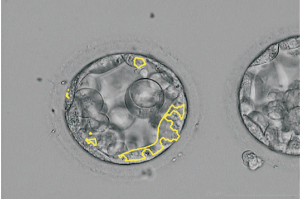
Table 3.3: Three example (best, average and worst case scenarios) outputs of the proposed algorithm along with the GT and difference between the two for sample images for grade B TEs.

Proposed Method	Ground Truth	Difference	Accuracy [%]
			100
			85.34
			43.35

represents the quality of the results and in each case we show the best, the average, and the worst results. We think that such information may provide some perspective for the readers of this paper. The third column, Proposed method, shows the visual presentation of the output regions generated by our algorithm. The boundaries of the detected TE regions are shown with red lines. The column of Ground Truth demonstrates the ground truth, which are manually marked with green lines by our experts.

Column Difference depicts the difference between the output of our algorithm and the GT. Finally, the column Accuracy, lists the computed shape accuracy in each case in percentage.
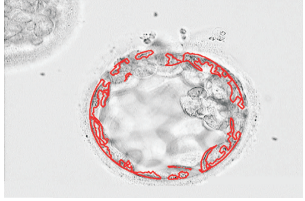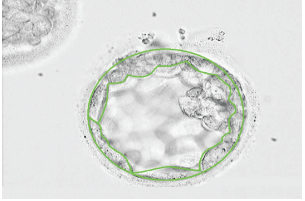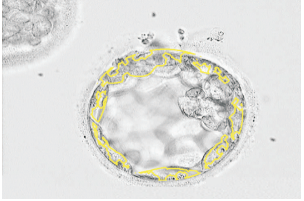
Table 3.4: Three example (best, average and worst case scenarios) outputs of the proposed algorithm along with the GT and difference between the two for sample images for grade C TEs.

Proposed Method	Ground Truth	Difference	Accuracy [%]
			100
			90.14
			74.63

3.6.4 Quantitative Evaluation

After the segmentation of TE regions, we compute the accuracy of the segmentation by comparing our results with the ground truth (GT). We have generated ground truth masks for all the embryo images based on the manual segmentation done by our expert embryologists. Fig. 3.10 show a sample case, where the GT mask (a) and the TE region found by our algorithm (b), are displayed next to each other.

To evaluate the proposed method quantitatively, we have used the McKeowns shape

(a)   (b)
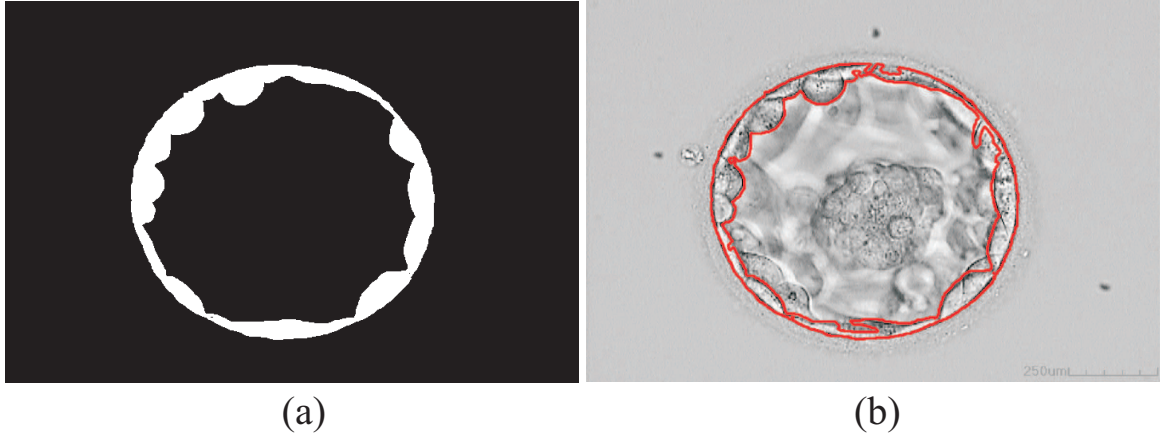
Figure 3.10: TE region masks (a) marked by the expert (b) identified by the proposed algorithm automatically.

accuracy factor [71] using the following equation:

$$TE_s = 1 - \frac{|A_{GT} - A_{TE}|}{A_{GT}} \tag{3.41}$$

Here the area of TE region in the ground truth (A_{GT}) is compared against the area of the automatically detected TE region by our proposed algorithm (A_{TE}). In addition to shape accuracy, additional metrics are required to obtain a complete assessment as errors of pixel labeling are not taken into account in the shape accuracy. Therefore three metrics of correctness, completeness, and overall quality are computed. Correctness measures the degree to which detected TE pixels are indeed TE pixels, whereas completeness measures the degree to which true TE pixels are detected by the system. Overall quality is normalization between the previous two.

$$Correctness = \frac{TP}{TP + FP} \tag{3.42}$$

$$Completeness = \frac{TP}{TP + FN} \tag{3.43}$$

$$OverallQuality = \frac{TP}{TP + FP + FN} \tag{3.44}$$

here, TP represents true positives (correctly extracted TE pixels), FP false positives (incorrectly extracted TE pixels), and FN false negatives (missed TE pixels). Optimal values for the four metrics are 1, and the Overall Quality cannot be higher than neither Correctness nor Completeness. The shape accuracy in % for each grade is shown in Table 3.5.

Table 3.5: Shape accuracy of TE regions for 85 test images.

Grade	No. of images tested	Mean Shape Accuracy [%]	Min/Max Shape Accuracy [%]
A	32	84.64	27.38/100
B	41	88.98	43.35/100
C	12	91.72	74.63/100
Total	85	87.75	27.38/100

Table 3.6 represents correctness, completeness and overall quality measures for our dataset of 85 images.

Table 3.6: Quantitative results for 85 test blastocyst images

Blastocyst Grade	Mean Shape Accuracy[%]	Mean Correctness [%]	Mean Completeness [%]	Mean Overall Quality [%]
A	84.6	79.8	74.2	67.6
B	88.9	85.5	82.3	76.8
C	91.7	84.6	78.4	72.3
Combined	87.7	83.3	78.7	72.7

In Fig. 3.11, the results of the shape accuracy measure is plotted against the grade of ZP. We wanted to see if the algorithm has any bias toward the level of expansion. From these results, we could not see any bias. However, we still thought that it might be informative to show these results as they highlight the distribution of our image dataset.

We also present the results of the shape accuracy measure plotted against the cavity area in pixels as shown in Fig. 3.12. The area of the cavity was manually computed. The aim of this analysis was to see if the algorithm has any bias toward the level of expansion in cavity area. In this case as well, no definitive pattern was observed.

In [16], Filho *et al.* proposed a semi-automatic system for classification of TE grades in day 5-human blastocysts. In their work, authors identify the TE's inner boundaries using Li *et al.* [42] variational level set. The initialization of the level set was performed manually.
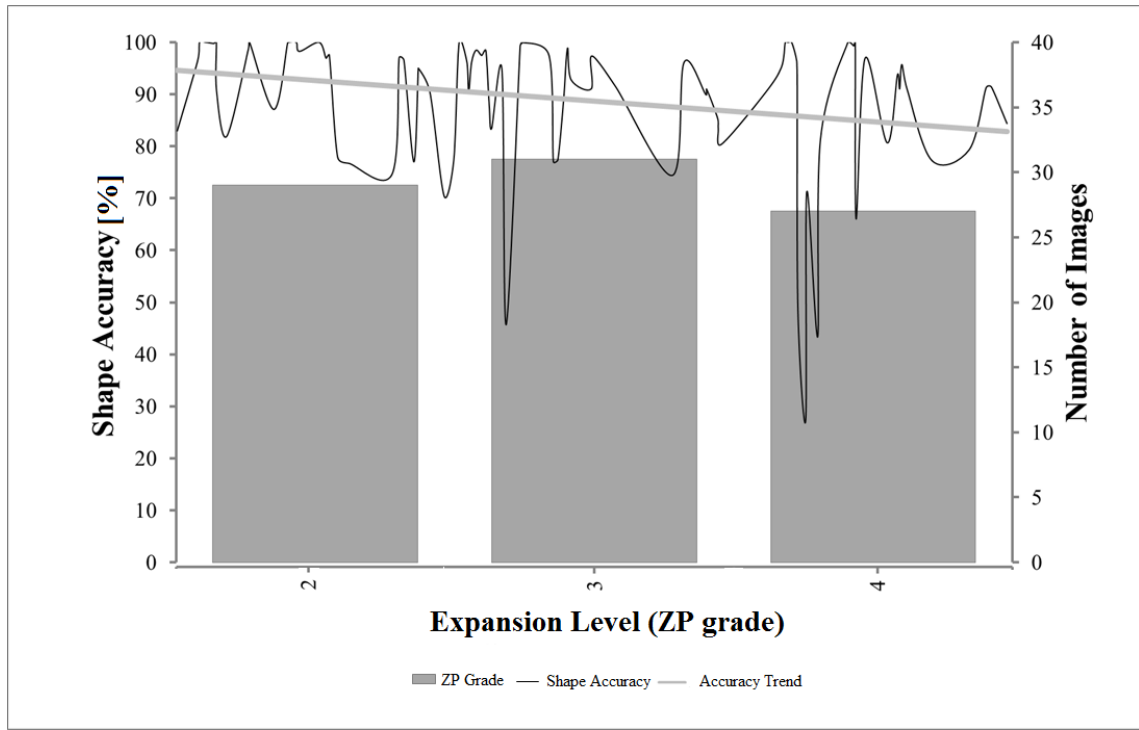
Figure 3.11: The Shape Accuracy for all the tested data against the level of expansion of the embryos or ZP thickness.

They estimated the TE region as the area confined by the ZP's inner and TE's inner boundaries. Once the TE region was extracted, fractal dimension of the signal was calculated and used to approximate the regularity of the TE thickness. The fractal dimension was utilized as a feature by SVM algorithm to classify (or grade) the TE. They report a classification accuracy of 0.53 and 0.92 for TE grades of b and c respectively.

The main focus of the proposed work by Filho [16] is the classification of grades, for which the area of the TE region is segmented semi-automatically. Since, the classification accuracy depends on the fractal dimension of the TE region, it is vital to estimate the TE area as accurate as possible. However, an automated algorithm for accurate identification of TE region plays a crucial role in a complete analysis of embryos during the growth period and it provides more details about the growth dynamics and therefore, eliminates interpolation of the knowledge from discrete observations.

The method proposed in this paper is capable of segmenting the TE automatically in
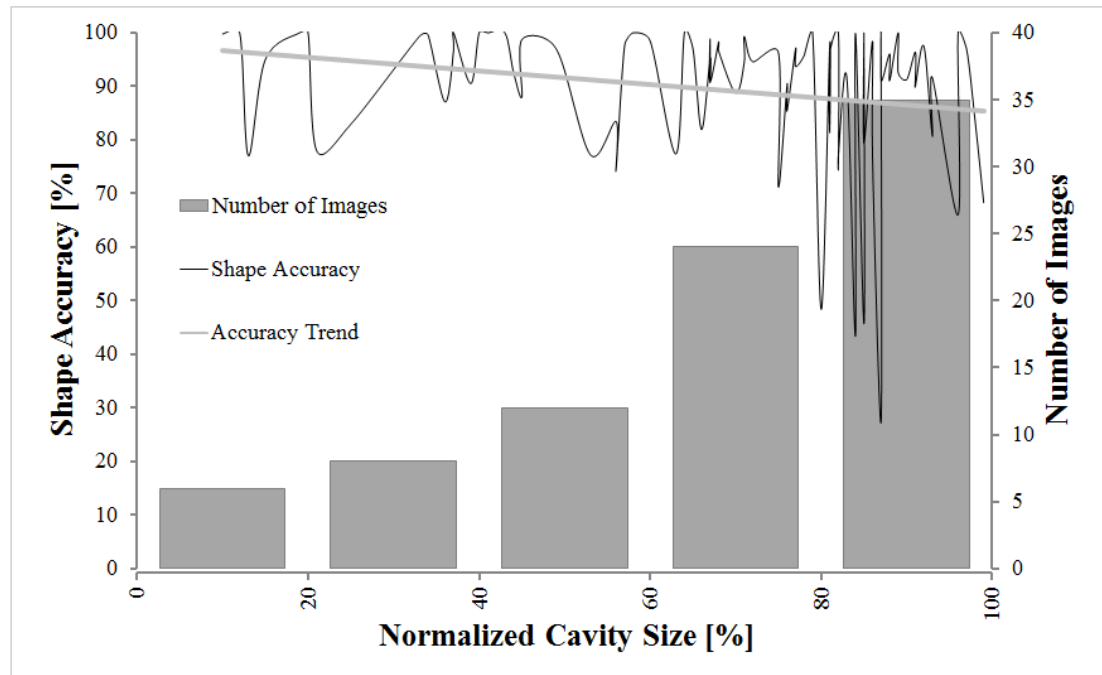
Figure 3.12: The Shape Accuracy for all the tested data against the normalized cavity size.

the presence of inhomogeneities in the cavity region and debris in the neighborhood. To our best knowledge, this is the first time that a fully automated method for segmentation of the TE in human's blastocyst is reported. We believe that our algorithm can be used in systems such as the one proposed by Filho to automate and remove the requirement for human intervention as much as possible. Removal of the debris through the Retinex algorithm [43] plays a critical role and facilitates extraction of the true boundaries using an advanced level set [44].

The proposed system can effectively and automatically segment TE regions in blastocyst images of grades A, B and C. We require only one condition in which the size of the embryo of interest must be larger than the remaining embryos in the image. We have tested our method on a dataset of 85 images and have been able to achieve a segmentation accuracy of 84.64% for grade A, 88.98% for grade B and 91.72% for grade C embryos. To our best knowledge, the presented results in here are the best reported results for the segmentation of Trophectoderm regions.

Chapter 4

Conclusions

In this thesis, two algorithms were developed to automatically identify two different components of human embryos at past time different growth times.

The first method focused on finding ellipsoidal models that represent blastomeres from day-1 and day-2 in HMC images of human embryos with no prior knowledge about the exact number of cells or their sizes, level of fragmentation, occlusion and overlap. The image is first divided into regions representing blastomeres using isoperimetric graph segmentation. The generated regions as a result of this segmentation were mapped to individual blastomeres. These regions were merged with their neighbouring regions using a new proposed region merging technique. Ellipsoidal models were further fitted to the regions using a least-squared error minimization method. We showed results and presented the overall accuracy through a set of 40 test images. The average segmentation accuracy was 80%. Most blastomers can be successfully identified in the image. In some cases, although the blastomers are correctly identified, there is an offset in the location, and theie shape might have identified to be smaller than the real size.

The second method aims to segment trophectoderm (TE) from day 5 blastocyst images with no prior knowledge. In the first step, debris inside and outside the cavity is removed using Retinex algorithm. Level-set is further applied to segment TE from the rest of the embryo regions. In cases where the ICM is connected to the TE, level-set algorithm extracts the combined TE and ICM mass. A K-Means algorithm was then applied to separate TE regions from such mass. We presented several examples and highlighted the accuracy of our method (88%) using 85 test images. Width of the segmented TE can be further computed and used as a measure to assess the quality of a human embryo.

4.1 Summary of Contributions

In this thesis, the following contributions are made:

4.1.1 Blastomere Extraction

The proposed algorithm in the 2nd chapter, is the first reported method capable of extracting blastomers only using image processing and computer vision. Our method does not require any specific prior knowledge and also produce better results (80%) comparing to the state of the art by Giusti *et al* [21] (71%).

4.1.2 Trophectoderm Segmentation

The proposed algorithm in the 3rd chapter, is the first reported method that can effectively segment the trophectoderm of all grades automatically. The previous algorithms manually removed the debris from the cavity and initialized the level-set in the close proximity, allowing it to converge to TE boundaries. The proposed method, however, overcame these limitations as it automatically eliminates the inhomogeneities of the blastocysts surface using the Retinex theory. In addition, an improved level-set capable of handling intensity inhomogeneties was used which made the proposed algorithm robust to some level of illumination variation and intensity inhomogeneities.

4.2 Future Research

For the future direction of the research, we identify the following areas of improvement for the overall system. The improvements are listed separately for each method.

4.2.1 Blastomere Extraction

1. Developing a sampling algorithm to select only ellipses that satisfy some satisfying pre-defined conditions of shape and size. This will improve the computational complexity of the algorithm.

2. Improving the region merging algorithm so that it can automatically select the weight for each feature. Currently we used a training set and these values are set for all the

data. Customizing these weights automatically for each image can certainly improve the overall quality of the recognition.

3. Improving the integrity of the used edge detection method, as the quality of the ellipses generated in the blastomere extraction method depends heavily on the quality of the detected edges.

4. Implementing the blastomere extraction algorithm in C/C++ will allow to process input images faster and for our work to be more suitable for processing time-lapse series images. Such image series often includes thousands of images.

4.2.2 Trophectoderm Segmentation

1. Improving the Retinex algorithm so that it can automatically choose the smoothing threshold for each image.

2. Using the texture and other local features of TE in addition to the image gradient to improve the segmentation accuracy.

3. Using the enhanced moving K-Means instead of standard K-Means to allow better separation of TE from ICM.

4. Implementing the level-set algorithm in C/C++ for faster convergence that lead to improvement in the computational complexity of the algorithm and its applicability to the time-lapse series images.

Bibliography

[1] A.N. Andersen, V. Goossens, A.P. Ferraretti, S. Bhattacharya, R. Felberbaum, J. de'Mouzon and K.G. Nygren. Assisted reproductive technology. *Human Reproduction*, volume 23: pages 756-771, 2008.

[2] J.G. Bromer and E. Seli. Computer-controlled, multilevel, Assessment of embryo viability in assisted reproductive technologies: shortcomings of current approaches and the emerging role of metabolomics. *Current Opinion in Obstetrics and Gynecology*, volume 20: pages 234-241, 2008.

[3] K. Niakan, J. Han, R.A. Pedersen, C. Simon and R.A. Pera. Human pre-implantation embryo development. *Development Biology*, volume 139: pages: 829-841, 2012.

[4] R.R. Angell, J. Xian and J. Keith. Chromosome anomalies in human oocytes in relation to age. *Human Reproduction*, volume 8: pages 1047-1054, 1993.

[5] M. Cruz , B. Gadea, N. Garrido, K.S. Pedersen, M. Martinez, I. Perez-Cano, M. Munoz and M. Meseguer. Embryo quality, blastocyst and ongoing pregnancy rates in oocyte donation patients whose embryos were monitored by time-lapse imaging. *Journal of Assisted Reproduction and Genetics*, volume 28: pages 569-573, 2011.

[6] F.D. Houghton, P.G. Humpherson, J.A. Hawkhead, C.J. Hall and H.J. Leese. Na+, K+, ATPase activity in the human and bovine preimplantation embryo. *Development Biology*, volume 263: pages 360-366, 2003.

[7] T. Hardarson, C. Hanson, A. Sjogren and K. Lundin. Human embryos with unevenly sized blastomeres have lower pregnancy and implantation rates: indications for aneuploidy and multinucleation. *Human Reproduction*, volume 16: pages 313-318, 2001.

[8] D.K. Gardner, E. Surrey, D. Minjarez, A. Leitz, J. Stevens and W.B. Schoolcraft. Single blastocyst transfer: a prospective randomized trial. *Fertility and Sterility*, volume 81(3): pages 551-555, 2004.

[9] D. Ben-Yosef, A. Amit, F. Azem, T. Schwartz, T. Cohen, N. Mei-Raz, A. Carmon, J. B. Lessing and Y. Yaron. Prospective randomized comparison of two embryo culture systems: P1 medium by Irvine Scientific and the Cook IVF Medium. *Journal of Assisted Reproduction and Genetics*, volume 21: pages 291-295, 2004.

[10] L. Scott, R. Alvero, M. Leondires and B. Miller. The morphology of human pronuclear embryos is positively related to blastocyst development and implantation. *Human Reproduction*, volume 15: pages 2394-2403, 2000.

[11] F. Puissant, M.V. Rysselberghe, P. Barlow, J. Deweze and F. Leroy. Embryo scoring as a prognostic tool in IVF treatment. *Human Reproduction*, volume 2: pages 705-708, 1987.

[12] C. Staessen, M. Camus, N. Bollen, P. Devroey and A.V. Steirteghem. The relationship between embryo quality and the occurrence of multiple pregnancies. *Fertility and Sterility*, volume 57: pages 626-630, 1992.

[13] C.V. Steer, C.L. Mills, S.L. Tan, S. Campell and R.G. Edwards. The cumulative embryo score: a predictive embryo scoring technique to select the optimal number of embryos to transfer in an in-vitro fertilization and embryo transfer program. *Human Reproduction*, volume 7: pages 117-119, 1992.

[14] S. Ziebe, K. Petersen, S. Lindenberg, A.G. Andersen, A. Gabrielsen and A.N. Andersen. Embryo morphology or cleavage stage: how to select the best embryos for transfer after in vitro fertilization. *Human Reproduction*, volume 12: pages 1545-1549, 1997.

[15] A. Dokras, I.L. Sargent, C. Redman and D.H. Barlow. Sera from women with unexplained infertility inhibit both mouse and human embryo growth in vitro. *Fertility and Sterility*, volume 60: pages 285-292, 1993.

[16] E.F. Santos, J.A. Noble, M. Poli, T. Griffiths, G. Emerson and D. Wells. A method for semi-automatic grading of human blastocyst microscope images. *Human Reproduction*, volume 127(9): pages 2641-2648, 2012.

[17] M.C. Magli, L. Gianaroli, A.P. Ferraretti, M. Lappi, A. Ruberti and V. Farfalli. Embryo morphology and development are dependent on the chromosomal complement. *Fertility Sterility,* volume 87(3): pages 534-541, 2007.

[18] C.C. Wong, K.E. Loewke, N.L. Bossert, B. Behr, C.J. Jonge, T.M. Baer and R.A. Reijo Pera. Non-invasive imaging of human embryos before embryonic genome activation predicts development to the blastocyst stage. *Nature Biotechnology*, volume 28(10): pages 1115-1121, 2010.

[19] Y. Tian, Y. Yin, F. Duan, W.Z. Wang, W. Wang, and M. Zhou. Automatic Blastomere Recognition from a Single Embryo Image. *Computational and Mathematical Methods in Medicine*, volume 2: pages: 1-7, 2014.

[20] U.D. Pedersen, O.F. Olsen and N.H. Olsen. A multiphase variational level set approach for modelling human embryos. In *2nd IEEE Workshop on variational, Geometric and Level Set Methods,* pages 25-32, 2003.

[21] A. Giusti, G. Corani, L. Gambardella, C. Magli and L. Gianaroli. Blastomere segmentation and 3D morphology measurements of early embryos from hoffman modulation contrast image stacks. In *IEEE international conference on Biomedical imaging: from nano to Macro,* pages 1261-1264, 2010.

[22] A.F. Frangi, W.J. Niessen, K.L. Vincken and M.A. Viergever. Multiscale vessel enhancement filtering. In *International Conference on Medical Image Computing and Computer Assisted Intervention,* pages 130-137, 1998.

[23] Rhys Lewis. Practical Image Processing. Ellis Horwood Limited, 1990.

[24] Y. Boykov and V. Kolmogorov. An experimental comparison of min-cut/max-flow algorithms for energy minimization in vision. *IEEE Transactions Pattern Analysis and Machine Intelligence*, volume 26(9): pages 1124-1137, 2004.

[25] A. Goldberg and R. Tarjan. A new approach to the maximum flow problem. *Journal of the Association for Computing Machinery*, volume 35(4): pages 921-940, 1988.

[26] L. Grady and E. Schwartz. Isoperimetric Graph Partitioning for Image Segmentation. *IEEE Transactions on Pattern Analysis and Machine Intelligence,* volume 28(3): pages 469-475, 2006.

[27] G. Karypis and V. Kumar. A fast and high quality multilevel scheme for partitioning irregular graphs. *SIAM Journal on Scientific Computing,* volume 20(1): pages 359-393, 1998.

[28] S. Wang and J.M. Siskund. Image Segmentation with Ratio Cut. *IEEE Transactions Pattern Analysis and Machine Intelligence*, volume 25(6): pages 675-690, 2003.

[29] M. Fiedler. Special Matrices and Their Applications in Numerical Mathematics. *Dover Publications*, 1986.

[30] B. Mohar. Isoperimetric numbers of graphs. *Journal of Combinatorial Theory*, volume 47: pages 274-291, 1989.

[31] N. Biggs. Algebraic Graph Theory. *Cambridge Tracts in Math*, volume 67, 1974.

[32] R. Merris. Laplacian matrices of graphs: A survey. *Linear Algebra and its Applications*, volume 197: pages 143-176, 1994.

[33] P. Perona and J. Malik. Scale space and edge detection using anisotropic diffusion. *IEEE Transactions on Pattern Analysis and Machine Intelligence,* volume 12(7): pages 629-639, 1990.

[34] R. Haralick. Digital step edges from zero crossing of second directional derivatives. *IEEE Transactions on Pattern Analysis and Machine Intelligence*, volume 6(1): pages 58-68, 1984.

[35] A. Fitzgibbon, M. Pilu and R. Fisher. Direct least-square fitting of ellipses. *IEEE Transactions on Pattern Analysis and Machine Intelligence*, volume 21(5): pages 476-480, 1999.

[36] P. Bourke. Calculating the area and centroid of a polygon. *Available at: http://astonomy.swin.edu.ac.uk/ pbourke/*, 1988.

[37] D.K. Gardner and W. B. Schoolcraft. Culture and transfer of human blastocysts. *Current Opinion in Obstetrics and Gynecology,* volume 11(3): pages 307-311, 1999.

[38] P.G. Crosignani. Multiple gestation pregnancy. *Towards Reproductive Certainty: Infertility and Genetics Beyond*, volume 15(7): pages 1856-1864, 2000.

[39] A. Ahlstrom, C. Westin, E. Reismer, M. Wikland and T. Hardarson. Trophectoderm morphology: an important parameter for predicting live birth after single blastocyst tranfer. *Human Reproduction*, volume 26(12): pages 3289-3296, 2011.

[40] A.E.B. Bendus, J.F. Mayer, S.K. Shipley and W.H. Catherino. Interobserver and intraobserver variation in day 3 embryo grading. *Fertility and Sterility,* volume 86(6): pages 1608-1615, 2006.

[41] C. Hnida, E. Engenheiro and S. Ziebe. Computer-controlled, multilevel, morphometric analysis of blastomere size as biomarker of fragmentation and multinuclearity in human embryos. *Human Reproduction*, volume 19(2): pages 288-293, 2004.

[42] C. Li, C. Xu, C. Gui and D.F. Martin. Level Set Evolution without Re-Initialization: A New Variational Formulation. In *IEEE Computer Society Conference on Computer Vision and Pattern Recognition,* pages 430-436, 2005.

[43] J. Morel, A.B. Petro and C. Sbert. A PDE Formalization of Retinex Theory. *IEEE Transactions on Image Processing,* volume 19(11): pages 2825-2837, 2010.

[44] C. Li, R. Huang, Z. Ding, J. Gatenby, N. Metaxas and J. Gore. A level set method for image segmentation in the presence of intensity inhomogeneities with application to MRI. *IEEE Transactions on Image Processing,* volume 20(7): pages 2007-2016, 2011.

[45] J.D. Cohen, R.F. Simons, R.G. Edwards, C.B. Fehilly and S.B. Fishel. Pregnancies following the frozen storage of expanding human blastocysts. *Journal of In Vitro Fertilization and Embryo Transfer,* volume 2(2): pages 59-64, 1985.

[46] A. Dokras, I.L. Sargent and D.H Barlow. Human blastocyst grading: an indicator of developmental potential? *Human Reproduction,* volume 8(12): pages 2119-2127, 1993.

[47] H.K. Zhao, T. Chan, B. Merriman and S.A. Osher. Variational Level Set Approach to Multiphase Motion. *Journal of Computational Physics,* volume 127(1): pages 179-195, 1996.

[48] A. Karlsson, N. Overgaard and A. Heyden. A Two-Step Area Based Method for Automatic Tight Segmentation of Zona Pellucida in HMC Images of Human Embryos. *Scale Space and PDE Methods in Computer Vision,* volume 3459: pages 503-514, 2005.

[49] D.A. Morales, E. Bengoetxea and P. Larranaga. Automatic Segmentation of Zona Pel-lucida in Human Embryo Images Applying an Active Contour Model. In *Medical Image Understanding and Analysis*, pages 209-213, 2008.

[50] J. Canny. A Computational Approach to Edge Detection. *IEEE Transactions on Pattern Analysis and Machine Intelligence,* volume 8(6): pages 679-698, 1986.

[51] E.F. Santos, J. A. Noble and D. Wells. Toward a method for automatic grading of microscope human embryo images. In *IEEE International Symposium on Biomedical Imaging: From Nano to Macro*, pages 1289-1292, 2010.

[52] E.H. Land and J.J. McCann. Lightness and retinex theory. *Journal of the Optical Society of America,* volume 61(1): pages 1-11, 1971.

[53] V. Agarwal, B.R. Abidi, A.F. Koschan and M.A. Abidi. An Overview of Color Constancy Algorithms. *Journal of Pattern Recognition Research,* volume 1(1): pages 42-54, 2006.

[54] L. Lei, Y. Zhou and J. Li. An investigation of Retinex algorithms for image enhance-ment. *Journal of Electronics,* volume 24(5): pages 696-700, 2007.

[55] E. Provenzi, L. DeCarli, A. Rizzi and D. Marini. Mathematical definition and analysis of the Retinex algorithm. *Journal of the Optical Society of America,* volume 22(12): pages 2613-2621, 2005.

[56] D.H. Brainard and B.A. Wandell. Analysis of the Retinex theory of color vision. *Journal of the optical society of America,* volume 3(10): pages 1651-1661, 1986.

[57] T.G. Stockham. Image processing in the context of a visual model. *Proceedings of the IEEE,* volume 60(7): pages 828-842, 1972.

[58] J. Frankle and J. McCann. Method and Apparatus for Lightness Imaging, *U.S. Patent,* 1983.

[59] F. Brian, C. Florian and J. Mccann. Retinex in Matlab. In *SID Eighth Color Imaging Conference: Color Science, Systems and Applications,* pages 112-121, 2000.

[60] K.P. Horn. Determining Lightness from an Image. *Computer Graphics and Image Processing,* volume 3(1): pages 277-299, 1974.

[61] G.R. Grimmett and D.R. Stirzaker. Probability and random processes: problems and solutions. *Oxford science publications*, 1992.

[62] P. Perez, M. Gangnet and A. Blake. Poisson image editing, *ACM Transactions on Graphics,* volume 22(3): pages 313-318, 2003.

[63] V. Caselles, F. Catte, T. Coll and F. Dibos. A geometric model for active contours. *Numerische Mathematik*, volume 66: pages 1-31, 1993.

[64] R. Malladi, J.A. Sethian and B. Vemuri. Shape modeling with front propagation: A level set approach. *IEEE Transactions on Pattern Analysis and Machine Intelligence*, volume 17(2): pages 158-175, 1995.

[65] L.D. Cohen. On Active Contour Models and balloons. *Computer Vision and Image Understanding*, volume 53: pages 1-18, 1991.

[66] D. Mumford and J. Shah. Optimal approximations by piecewise smooth functions and associated variational problems. *Communications on Pure and Applied Mathematics*, volume 42(5): pages 577-685, 1989.

[67] A. Tsai, A. Yezzi and A.S. Willsky. Curve evolution implementation of the Mumford-Shah functional for image segmentation, denoising, interpolation, and magnification. *IEEE Transactions on Image Processing*, volume 10(8): pages 1169-1186, 2001.

[68] L. Vese and T. Chan. A multiphase level set framework for image segmentation using the Mumford and Shah model. *International Journal of Computer Vision*, volume 50(3): pages 271-293, 2002.

[69] T. Chan and L. Vese. Active contours without edges. *IEEE Transactions on Image Processing*, volume 10(2): pages 266-277, 2001.

[70] S. Theodoridis and K. Koutroumbas. Pattern Recognition. Third Edition, *Academic Press,* 2006.

[71] D.M. McKeown, T.M. Bulwinkle, S. Cochran, W. Harvey, C. McGlone and J.A. Shufelt. Performance evaluation for automatic feature extraction. *International Archives of Photogrammetry and Remote Sensing,* volume 33(2): pages 379-394, 2000.